QUANTITATIVE PHASE ANALYSIS IN LENSLESS DIGITAL INLINE HOLOGRAPHIC MICROSCOPY

A Thesis Submitted to
the Graduate School of Engineering and Sciences of
İzmir Institute of Technology
in Partial Fulfillment of the Requirements for the Degree of

MASTER OF SCIENCE

in Photonics Science and Engineering

by
Ali Aslan DEMİR

July 2021
İZMİR

ACKNOWLEDGMENTS

I will start with one of the famous quotes of Rumi. "It’s your road and yours alone. Others may walk it with you, but no one can walk it for you." Yep, it's true, we are all alone while building up our roads. But without someone to guide us during these roads, we might all lost the way I lost during my bachelor's while struggling with theoretical physics. It took some time for me to understand which way that I want to go. During this indetermination, I met with my advisor Assoc. Prof. Dr. Hüseyin Cumhur TEKIN. I would like to thank him for opening the doors of Bioengineering roads for me. During this road, I have learned many precious things from him that I will use for the rest of my life.

Secondly, I would like to thanks my dear friend Kerem Delikoyun for spending even the most meaningless activities and conversations with me. Without him, I was not able to widen my intuition in different directions. Also, special thanks to members of the Laboratory of Biomedical Micro and Nanosystems for the good activities that we had and their valuable ideas.

I learn a lot from the studies of Tatiana Latychevskaia and the articles of Aydogan Ozcan's research group. Special thanks for their valuable contributions in the area of inline holography.

Most importantly, I would like to thanks my family for being such a supportive during my whole academic career without asking the reasons. Also, starting from my closest to the rest of my friends, thanks for you all. Sorry, but I am not going to write your names one by one.

I would like to thank The Scientific and Technological Research Council of Turkey (TÜBİTAK, the grant #119M052) and Iztech Scientific Research Project (2021İYTE-1-0095) for their financial support during my master's studies.

ABSTRACT

QUANTITATIVE PHASE ANALYSIS IN LENSLESS DIGITAL INLINE HOLOGRAPHIC MICROSCOPY

Computational imaging modalities replace the bulky, complex, and expensive optical components of traditional imaging procedures with numerical reconstruction steps. Digital holographic microscopy is one of the most prominent ones with the possibility of obtaining quantitative phase information by measuring the phase shift change caused by the refractive index of objects. In the lensless digital holographic microscopy system, a pinhole and a light-emitting diode are sufficient to create a holographic pattern on the camera sensor. Here, the optimization of a digital lensless inline holographic microscopy setup was performed to obtain optimal phase value. Also, to retrieve the lost phase information during the recording step, the numerical solution was performed with the single and multi-shot phase retrieval methods. Then, human breast adenocarcinoma (MDA-MB-231) and human myeloid leukemia (U937) cells were analyzed to obtain phase shift, perimeter, and circularity values. These parameters were used to obtain a quantitative differentiation model to replace the traditional labeling or visual confirmation steps with a direct analysis manner. The analysis of respective cells with the classification, object detection, and conditional generative adversarial models can be used directly with pre-trained weights to lessen the computational workloads. With this study, the quantitative analysis with lensless holographic microscopy setup was shown to be a label-free differentiation mechanism to separate cancer cells from monocytes cells which could be used for the early diagnosis of cancer. Also, the proposed method has the potential to be used to identify other cells with links to the diagnosis of different diseases.

ÖZET

MERCEKSİZ DİJİTAL SIRALI HOLOGRAFİK MİKROSKOPTA KANTİTATİF FAZ ANALİZİ

Hesaplamalı görüntüleme modaliteleri, geleneksel görüntüleme prosedürlerinin hacimli, karmaşık ve pahalı optik bileşenlerini sayısal yeniden yapılandırma adımlarıyla değiştirir. Dijital holografik mikroskopi, nesnelerin kırılma indisinin neden olduğu faz kayması değişimini ölçerek nicel faz bilgisi elde etme olasılığı ile en öne çıkanlardan biridir. Lenssiz dijital holografik mikroskopi sisteminde, kamera sensörü üzerinde bir holografik desen oluşturmak için bir iğne deliği ve bir ışık yayan diyot yeterlidir. Burada, optimum faz değerini elde etmek için dijital lenssiz sıralı holografik mikroskopi kurulumunun optimizasyonu yapıldı. Ayrıca, kayıt aşamasında kaybolan faz bilgisini geri getirmek için tekli ve çok atışlı faz alma yöntemleri ile sayısal çözüm gerçekleştirilmiştir. Daha sonra insan meme adenokarsinomu (MDA-MB-231) ve insan miyeloid lösemi (U937) hücreleri analiz edilerek faz kayması, çevre ve dairesellik değerleri elde edildi. Bu parametreler, geleneksel etiketleme veya görsel doğrulama adımlarını doğrudan analiz yöntemiyle değiştirmek için nicel bir farklılaşma modeli elde etmek için kullanıldı. Sınıflandırma, nesne algılama ve koşullu üretici çekişmeli modelleri ile ilgili hücrelerin analizi, hesaplama iş yüklerini azaltmak için önceden eğitilmiş ağırlıklarla doğrudan kullanılabilir. Bu çalışma ile, lenssiz holografik mikroskopi düzeneği ile kantitatif analizin, kanser hücrelerini monosit hücrelerinden farklılaştırma için kanserin erken teşhisinde kullanılabilecek bir etiketsiz ayrıştırma mekanizması olduğu gösterildi. Ayrıca önerilen yöntem, farklı hastalıkların teşhisiyle bağlantılı diğer hücrelerin tespitinde de kullanılma potansiyeline sahiptir.

"The answer to this is very simple. It was a joke. It had to be a number, an ordinary, smallish number, and I chose that one. Binary representations, base thirteen, Tibetan monks are all complete nonsense. I sat at my desk, stared into the garden and thought '42 will do' I typed it out. End of story."

Douglas Adams

TABLE OF CONTENT

LIST OF FIGURES

Figures **Page**

Figures **Page**

Figures **Page**

CHAPTER 1

INTRODUCTION

The curiosity of what is behind the unseen has always appealed to the interest of humanity. Towards the smallest details, it is all started with magnifying the objects with lenses. In the late 16th century, Hans and Zacharias Janssen built up the first compound microscope by using two aligned lenses to see the magnified version of objects (Lockyer 1976). It was primarily based on visible light to illuminate the object and obtaining the resulting image with magnifying lenses to direct the formed image into the eye or camera. Over time, technological advancements in optical microscopes help us to better visualize smaller objects with increased resolution and precision that can theoretically go down to 200 nm diffraction limit (Vangindertael et al. 2018). However, images taken from most of the microscopes remain as mostly qualitative results because the captured images are only representing the amplitude information of the objects ("The quest for quantitative microscopy" 2012). To obtain quantitative results, either image needs to be analyzed statistically or optical setups need to be much more complex with expensive components. For example, fluorescent microscopy can be used to visualize sub-cellular activities with increased precision. Especially with the invention of Super-Resolution Fluorescent Microscopes, diffraction limits have broken and interactions in sub-cellular regions started to be quantified (Vangindertael et al. 2018). However, particular tagging requires expertise with special materials in many conditions. Also, expensive components are required to be used mainly by expert technicians. That is why the usage of these new imaging modalities remains limited in research facilities.

In parallel to the recent progress in optical microscopes, some of the scientists' attention goes toward computational imaging modalities. In computational imaging modalities, the complexity of building complex, expensive and bulky setups are replaced with the numerical solution steps. Instead of using lenses to focus the formed image, computational imaging modalities based on the whole information captured by the camera sensor without the use of additional optical components (Hu et al. 2017). In this way; compact, portable, and cost-effective devices are started to appear on the stage. These computational point-of-care (POC) modalities enabled scientists to break down barriers of science from research facilities to global opportunities (Coskun and Ozcan 2014). Especially with the recent advancements in camera sensor and chip technologies, the usage of computational imaging modalities is boosted. The one that is related to eliminating the use of lenses with a simple light emitting diode (LED) and a pinhole is called lensless holography.

1.1 Lensless Digital Inline Holographic Microscopy

The key points of holography is actually gone back to double-slit experiment (Young 1802) and interferometry studies (Michelson and Morley 1887) to create interferometric patterns. At the beginning of the 1800s, Young performed a double-slit experiment to show the result of two interfering waves from double slits to obtain bright and dark fringes (Young 1802). In the same era, Michelson and Morrey have used a semi-silvered mirror to split incoming light into two different parts. By changing the respective distances between splitter to another mirror, the resulting bright and dark fringes are changed (Michelson and Morley 1887). Their study brings another important consequence with the interferometric applications to the life sciences. In theory, if you superimpose two waves coming from the same distance from different points, you will obtain perfectly aligned bright and dark interference patterns due to constructive and destructive interference. Depend on the optical path length difference between two different arms, you will obtain a difference in the resulted interference pattern. On the other hand, if you place an object in one of the incoming wave directions, it will obtain a shift in optical path length caused by a decrease in the speed of light. Therefore, the optical path length shift will create a difference in the recorded pattern specific to the object's characteristics. In this system, the incoming wave from the disturbing side is called the object wave, and the other undisturbed one is called the reference wave. Therefore, the main idea of holography uses a phase shift based on the resulting diffraction pattern of the object and reference waves.

Obtaining the phase shift information from imaging systems is first introduced with Gabor's studies on electron microscopy. In the past, lens-based systems are only capable of capturing amplitude information. However, with Gabor's Inline Holography, recording both amplitude and phase information directly from the wave-field formation is introduced, the term of holography came into the stage to represent the capturing the whole (amplitude and phase) interference information (GABOR 1948). The main advantage of this method lies in eliminating the optical aberrations and distortions caused by the use of lenses (Kim 2010). However, the acquisition of object images from captured whole information requires two main steps to be performed. At that time, the resultant wave-field information is captured by a photographic plate. Then, the obtained information is numerically reconstructed to get an actual image of the object. But during the reconstruction step, the twin-image phenomenon occurs to limit the accurate reconstruction and resolution of an object due to overlapped conjugate twin image terms.

To get a twin-free object image from holography, the initial studies are focused on optical solutions. The main solution comes from the interferometric studies with the use of off-axis holography applications to efficiently retrieve the phase information. Emmett N. Leith and Juris Upatnieks used a beam splitter to separate reference and object waves with

an off-axis holography setup by inducing a small tilt to eliminate twin image term (Leith and Upatnieks 1963). In the proposed idea, an object is illuminated separately with object wave and it superposes with the reference wave near the camera sensor by introducing a small tilting angle. The obtained frequency response and resulting reconstruction make it possible to differentiate real and twin images easily in the Fourier space. With this systematic, both quantitative information about the phase and sub-micrometer-scale resolutions can be achieved. Therefore, it promises a powerful tool for the diagnosis and quantification of diseases such as Malaria (Anand et al. 2012) or it can be used in live-cell imaging studies such as cancer (El-Schich, Leida Mölder, and Gjörloff Wingren 2018). On the other hand, the main disadvantage of such an optical setup remained as a challenge because the use of lenses and beam splitters are required in the off-axis systems which limit the widespread usage in research facilities.

In the case of Lensless Inline Holographic Microscopy, both waves come from the same direction by interfering with each other at the camera sensor. In such a setup, the main goal is to eliminate the use of lenses to make them more useful for resource-limited areas. Therefore, inline systematic have appealed a greater interest within scientists. Within this context, instead of focusing on the formed image, inline holography focused on the diffraction pattern to be able to obtain the required solution numerically. Therefore, the scope of off-axis and in-line holography is quite different. The comparison of their representative setups is given in Figure 1.1.a for off-axis holography and inline holography in Figure 1.1.b. In off-axis systems, beam splitter and mirror usage are necessary. Also, in order to maintain the coherency, the light source needs to be a laser. On the other hand, inline holography requires a coherent or partially coherent light source with a pinhole to create a diffraction pattern. The main components used in these systems are given in the Figure 1.1.c.

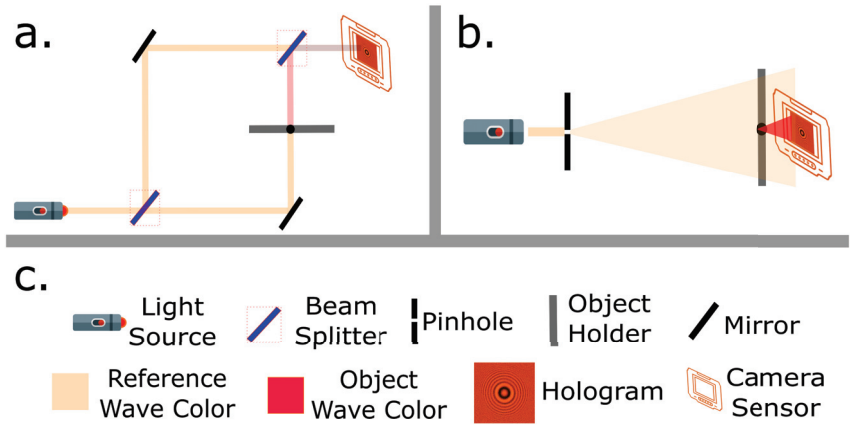

Figure 1.1: Illustrations of holographic microscopy setups. a. Off-axis holography. b. Inline holography. c. Optical components of these setups.

Since the captured hologram for the inline systematic are completely overlapped between object and reference wave, it is not directly possible to differentiate twin image terms. The required solution comes later with the phase retrieval process. On the other hand, the successful and effective implementations of both methods are irremediably evolved with the advancements of digital camera sensors and computational advancements.

Until digital camera sensors, holographic diffraction patterns are recorded by photographic plates and the reconstruction process remained a challenging task due to the usage of analog recording systems. However, the introduction of digital camera sensors has enabled the resulting wavefront to be captured digitally. The first applications of capturing and reconstruction of holograms by digital holography with conventional CCD cameras are introduced in 1994 by Schnars (Schnars and Jüptner 1994). Later on, quantitative studies with more efficient reconstruction steps in the area have been performed by Zhan et al. in 1998 (Zhang and Yamaguchi 1998). In addition to lessening the burden of the recording step, the computational reconstruction step started to be performed digitally thanks to the advancements in computing power associated with computers. After these studies, the effect of the digital developments has led digital holography to re-emerge in the area at the beginning of the 2000s (Xu et al. 2001). Especially, capturing the 3D quantitative information cost-effectively by eliminating the use of lenses catches the most valuable interest within scientists particularly towards the lensless inline holographic microscopy. The possibility of refocusing transparent samples along z-direction in different depths has found applications in life sciences (Peruhov and Mihaylov 2013). Since the obtained amplitude and phase information specific to the change of refractive index value within the cell, cellular quantification studies become easier to be implemented. The first biological applications of digital inline holography come with the tracking of algae and bacteria (Xu et al. 2001). Also, in situ studies about ocean planktons have been introduced with digital inline holographic microscopy setups (Garcia-Sucerquia et al. 2006). Later on, with the efforts of the same group, the possibility of tracking particles in 4D has been demonstrated with inline systematic (Garcia-Sucerquia et al. 2008). In the following year, Seo et al. introduced the Lensfree Holographic Ultra-wide-field Cell Monitoring Array Platform which allows imaging in wide-field platforms (Seo et al. 2009). In the same study, by using a pinhole size around $100\mu m$ for filtering, the spatial resolution of the system is increased by eliminating high-frequency components. These studies demonstrated the capability of lensless holographic imaging as a powerful tool. However, the effective solution to the inherent twin-image artifact has appeared on the stage much later.

1.2 Iterative Phase Retrieval

The image that we know from our daily lives to microscopic images are mainly recorded as in the spatial domain to represent features based upon amplitude measurements. But the phase information is more valuable in biological studies and direct evaluation of phase information is hard to interpret from captured images in the spatial domain. Instead of focusing the spatial domain applications, frequency components evaluation provides easily interpretable results to obtain phase information of objects. However, in some applications, it requires sophisticated optical setups with complex registration algorithms. The main idea to obtain such a piece of information lies upon obtaining the whole frequency components of an object. This can be achieved by taking the image from multiple directions even if it possible to obtain it from 360-degree measurements. But such methods require complex setups and therefore limiting the usage. On the other hand, the phase information of objects can be achieved by easy-to-use numerical solutions in Lensless Digital Inline Holographic Microscopy (LDIHM). Although the whole frequency components are not taken, the resultant phase value defines the actual sectional view of the object and its phase shift.

The usage area of lensless holographic microscopy is increased but the inherent twin image phenomena of Gabor's inline holography has remained a major problem in the reconstruction step for many years. Since the overlapped conjugate twin image terms suppressing the actual shape and sub-cellular information, it is very crucial to retrieve this information by phase retrieval process. Many practical and computational solutions have been introduced starting from the 1970s. As an optical solution, increasing the distance between the object and the camera sensor to reduce the twin image artifact signal is proposed. In this way, the effect of the twin image on the reconstructed object is minimized (Lai, Kemper, and Bally 2000). On the other hand, computationally effective solutions within this area come with the mostly known term called phase retrieval process (Hennelly et al. 2009). The first numerical solution for the phase retrieval process is introduced in 1972 by Gerchberg & Saxton (Gerchberg 1972). The proposed algorithm is based upon applying an iterative algorithm to retrieve the lost phase information during the reconstruction step to obtain accurate phase information and therefore eliminating the twin image term (Liu and Scott 1987). The required solution can be either deterministic or iterative. Deterministic processes based upon non-interferometric intensity gradient measurements to obtain accurate phase by Green's function (Teague 1983). The other and more common method uses an iterative phase retrieval method with a back and forth mechanism between recorded intensity diffraction pattern and obtained reconstruction plane or another intensity pattern (Fienup 1982). The main idea of such a retrieval lies in obtaining the accurate complex wavefunction in the object plane by introducing a

constraint to the system. The idea of applying such a constraint is based upon the fact there are multiple Fourier Transform relationship exists between the object plane and hologram plane to define an accurate Fourier relationship. With twin image presence, the number of unknown object functions is doubled therefore it becomes impossible to solve this problem by solely applying a reconstruction step. Therefore, the applied constraint reduces the number of unknowns in the iteration step to fasten the convergence of the required outcome (Greenbaum et al. 2012). In other words, this applied constraint will use the information from the object plane to understand how it can lead to the final formation of the hologram. At each iteration, applied constraint makes it possible to accurately lead to the final complex diffraction pattern by updating the complex pattern in the object plane with keeping the resultant hologram pattern constant in the hologram plane. Depend on the object size and applied constraint, the number of iterations can go from a few to hundreds of iterations. Since the main idea is to reduce the number of unknowns, multiple shots were taken to obtain phase retrieved images traditionally. But today, it is also possible to eliminate twin image artifacts with single-shot intensity measurement. However, due to the computational limitations, detailed studies have not been performed until the 2000s.

The advancements in digital sensors together with computers have enabled the phase-retrieval process to be performed in much more complex studies such as biological studies. First, effective solutions to the twin image problem in spherical wave conditions were introduced by means of a numerical reconstruction step with Tatiana and Fink in 2007 (Latychevskaia and Fink 2007). Later on, a detailed explanation about hologram simulation and reconstruction with the usage of spherical and plane wave approximations has been introduced (Latychevskaia and Fink 2015). In parallel studies, the iterative phase retrieval processes have been applied to biological applications to obtain accurate phase results with single-shot measurements (Mudanyali et al. 2010). These results have enabled lensless digital inline holographic microscopy to be used more widely in life science applications. On the other hand, the computational workload increased due to the complex nature of biological objects. Moreover, since the exact location of the reconstructed object is not known primarily during this reconstruction step, finding the best focus for the reconstruction step within the context of auto-focusing remained a challenging computational task. First numerical solutions to the auto-focusing problem are introduced in 2007 by using the l1 norm between real and twin images (Li et al. 2007). Later on, many detailed studies are performed to estimate the sharpest amplitude reconstruction point in the focus object plane (Dubois et al. 2006). Although much progress has been introduced in lensless holographic microscopy with effective solutions to these computational problems, computational workload with automatizing steps comes later with the usage of learning-based models.

1.3 Deep Learning

The analysis of a large amount of data in an efficient way is one of the main goals for today's scientific community in many areas. In the traditional image analysis models, the application of respective filters or processing steps is treated one by one with human intervention. Therefore, the analysis of a large amount of data became a huge problem with the technological developments after the 2000s. On the other hand, the importance of using neural networks for image analysis to lessen the burden of computing is increased within years (Kan 2017). By replacing the conventional image processing steps with self-learning neural networks, it becomes much easier to differentiate object structures with deep neural network models (Kraus, Ba, and Frey 2016). These deep learning models boosted with applications in biology and medicine to provide efficient healthcare solutions throughout the world (Meijering 2020).

The step towards the use of computational solutions by neural networks has been a little bit bumpy and it is all started in 1957 with the introduction of perceptron (Rosenblatt 1957). Along the way of neural network models, two winters have passed to limit their widespread usage and cut the incoming investments in the area. The first one arises about the doubts that are based on neural networks that cannot learn linearly in-separable problems (Minsky and Papert 1987). In the following years, error back-propagation was introduced to solve this in-separable problem with clever weight functions (Werbos 1975). The first building block of today's deep learning models are introduced with back-propagated handwritten digits in 1989 by Lecun et al by convolutional neural network models (LeCun et al. 1989). But the problem of vanishing or exploding gradient problem during backpropagation has been appeared to limit the usage of neural network models again in the 1980s that last up to the late 1990s. With the combined stochastic gradient model and improved backpropagation algorithm, a new solution was introduced in 1998 with a 7-level convolutional LeNet-5 model (Hochreiter 1998). Then, in 2006, deeper network models have provided scientists with faster computation with increased accuracy (Hinton, Osindero, and Teh 2006). The importance of analyzing the image efficiently with neural network models is boosted with the imagenet challenge in 2009 (Deng et al. 2009). Many efficient results have been introduced in the area of deep learning after this challenge to increase accuracy.

The typical structure of neural network models starts with taking the 2D brightness matrix of the captured image. In such an image, each pixel corresponds to the brightness value(0-255) of an 8-bit image. This image is formed depending on the absorption, scattering, and transmission properties of the object. The information comes from different parts of the object which represent the specific patterns. For the human eye, it is hard to differentiate these specific patterns. But the idea of the neural network model is to

use set up a model to reveal the unseen or barely seen differences that eventually lead to differentiate objects. In general, the model takes an image as an input and gives the output classes based upon the probability of belonging to the specific class. The learning process of such a model is based upon using a backpropagation algorithm to understand how the initial weights need to be changed to obtain the best results in the output. The most important benefit of such a model is that the neural network model learns the required changes on its own without any direct human interference (LeCun, Bengio, and Hinton 2015).

The most common neural network models are based upon a classification of images into different categories. For many years, achievements in this area are characterized by the Imagenet LSVRC-2010 dataset to effectively differentiate 1000 different classes with achievable maximum efficiency. By decreasing the prediction errors, many effective neural network models are introduced that are mainly using the convolutional neural network (CNN) models. Their uniqueness is based on using more deeper network model without saturation problem by introducing the dropout to regularize the performance (Deng et al. 2009).

In parallel to ongoing processes and applications of neural network models, the first effective usage of neural network models is introduced to holographic microscopy applications in 2017 (Sinha et al. 2017). The main efforts go toward obtaining phase recovered images in the reconstruction step (Rivenson et al. 2017). Later on, efficient auto-focusing with phase recovery step is introduced with deep learning model (Wu and Ozcan 2018). Also, the usage of lens-free holographic microscopy is eliminated the motion blur and recovered the phase information on a deep learning model with water samples are introduced with the studies of Göröcs et al.(Gorocs et al. 2018). More interesting usage of deep learning models in quantitative phase images is used for virtual label-free staining of pathology applications to provide efficient quantification results (Rivenson et al. 2019). Recently, a recurrent neural network model is used in the phase recovery step to obtain a better depth of field with increased image quality (Huang et al. 2021). Also, morphological evaluations of quantitative phase images have been performed to characterize cells (Lam et al. 2020).

In parallel to the advancements in classification models, neural network models are also focused to detect an object's position within the given image in terms of positional matrix values starting from the beginning of the 2000s (Viola and Jones 2001). However, it takes many years to apply object detection models with classification to both locate the position of the object and classify it into different classes. One of the primary efforts in this area is introduced with Szegedy et al. in 2013 (Szegedy, Toshev, and Erhan 2013) to tackle the bounding boxes problem as a regression task to effectively classify objects. The main idea comes from predicting a box that encloses the object and it is used to understand how well it is overlapped with the image. The standard metric in such models uses

Intersection Over Union (IoU) to understand this relationship. In 2014, a more efficient solution is proposed with Ross et al. (Girshick et al. 2014) to take classification problem by sliding window method to process the image. Their proposed Region based-CNN solution effectively increases the mean average precision (mAP) value. In 2015, Ren et al. (Ren et al. 2017) introduced a new version to combine Region Proposal Network (RPN) with Fast R-CNN model to obtain nearly cost-free region proposals. But the main problem associated with such models is their single evaluation-based pipeline to limit the processed frames per second. Alternatively, You Only Look Once (YOLO) is first introduced in 2015 to provide an alternative solution to object detection models to achieve real-time results (Redmon et al. 2016). When compared to traditional counterparts, YOLO takes an image by splitting it into a set of cell matrices. Therefore, the collective results from all of the objects are achieved in a single process with a much faster time.

In neural network models, the learning process is performed either by supervised or unsupervised models. Supervised learning models depend on human interruption to give biased data structure into learning models. Such a model can be used widely in Classification and Object Detection problems. On the other hand, generative adversarial models are considered unsupervised because the final analyzed data created during the learning process depends on the initial conditions. It does not use input data directly. Instead, it learns the feature maps to connect the relationship.

Another important usage of area of the deep learning applications are introduced with Goodfellow et al. in 2014 about the generative adversarial networks (GANs)(Goodfellow et al. 2014) One year later, deep convolutional generative adversarial models (DCGANs) are introduced with Radford et al. to prove such models would be more useful especially in unsupervised learning models(Radford, Metz, and Chintala 2016). GANs uses the principle of convolutional neural networks to combine two different neural network structure to generate predictions by learning the relationships of generated data. In the generative model, data distribution is achieved from input data and predictive results are feed-forward to the discriminator model. In the discriminator model, incoming data is used to classify predictive results as being real or fake. It can be characterized as a mutualist relationship to keep update the predictions until the best estimation is achieved(Hughes, Zhu, and Bednarz 2021). The possibility of using generative adversarial networks (GAN) to cross-match between brightfield images and holographic counterparts has also served as a bridge between brightfield and holographic imaging modalities (Wu et al. 2019).

Up to this point, a general introduction about inline holography with deep learning models and their applications is given. A chronological timeline of the progress of Lensless Holographic Microscopy with its usage in deep learning applications is given in the Figure 1.2.

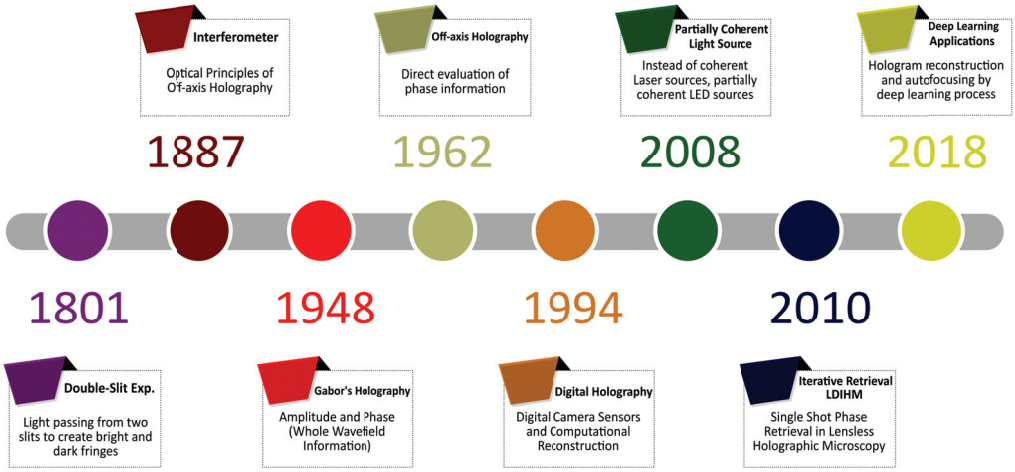

Figure 1.2: Timeline of the lensless holographic microscopy

1.4 Cancer Cell Detection

There is another advantage of lensless holographic microscopy exists which lies upon its possibility to be used as a point-of-care application to serve as a cytometer. In such a study, LDIHM could be used to early diagnose of cancer cells in vitro studies. Since one of the vital and primary numbers of deaths associated with the differentiation of cell structure is considered to be cancer, a cancer diagnosis is still an important area to focus on. It is estimated that almost 10 million deaths occurred in 2020 (Sung et al. 2021). Many treatment methods are introduced within the last era, but even the most efficient and prominent ones such as immunotherapy do not ensure 100% cure of cancer (Zhong et al. 2020). Due to this reason, the early diagnosis step is important to decrease the number of deaths. In the early stage of cancer, structural deformations have led cancer cells to become more aggressive and their number increases rapidly. These cells can metasthase to different organs that can increase the mortality rates (Fares et al. 2020). These cancer cells can penetrate through the blood flow is termed as circulating tumor cells (CTCs) and they are the main reason for metastasis (Rodrigues and Vanharanta 2019). Therefore, early-stage cancer cell detection can be conducted by identifying CTCs in the bloodstream. There have been a great number of studies performed in the field to detect cancer in the early stages of the disease (Raub and Nehmetallah 2017). Effective solutions come with cytometry-based methods to detect cancer cells within the blood flow. But this detection process has been a great challenge for many years because of the large number of cells within the blood flow, the rareness of CTCs, and the effect of exogenous markers (Lopresti et al. 2019). The first cytometric applications with inline holography are introduced in 2015 by Singh et al. by introducing a classifier to detect tumor cells within mixed solutions (Singh et al. 2017). Still, no direct applications of CTC detection within blood flow are

introduced due to the complex and heterogeneous structure of blood. So, this area still in the developing stage and it seems many effective solutions could be introduced very soon.

The diagnosis of cancer with machine learning algorithms is an active area and currently developing into real-time studies with effective neural network models. The applications of machine learning models in cancer studies improve the prediction accuracy as well as it is applied to prognosis studies to understand how the treatment can be much more efficient (Cruz and Wishart 2006). However, the heterogeneity of cancer cells especially poses a great challenge towards its detection (Delikoyun et al. 2021a). Past studies within this area are actually evolved from statistical gene expression studies to cellular identifications (Kourou et al. 2015). In their study, Triphaty et al.used a neural network model to identify breast cancer cells from segmented images (Tripathy, Mahanta, and Paul 2014). In their study, they have used MCF-7 and MDA-MB-231-MB-231 cancer cells with human normal breast cancer cells to obtain more than 95 percent accuracy. In 2019, Rubin et al. introduced a cell classification strategy to use a pre-trained generative adversarial model with transfer learning application to classify cancer cells from healthy ones. In their study, they have used off-axis holography with a small dataset to obtain more than 90 percent accuracy (Rubin et al. 2019). Therefore, they have opened the potential way for holographic imaging with machine learning to classify cell types in a label-free manner. Also, they show that such a system can be used in cytometry applications.

The first effective applications of digital holographic microscopy to cancer cells differentiation studies actually goes into 2009 with MCF-7 and MDA-MB-231-MB-231 to understand viability and density of cells (Ryle et al. 2009). Later on, machine learning models with LDIHM systems is introduced in 2015 to show the possibility of classification of blood cells to distinguish monocytes, granulocytes, and lymphocytes with accuracy close to 90 percent (Schneider et al. 2015). Recently, a more efficient neural network model is used to classify and use regression to breast cancer cells with cancer markers. The proposed Holonet model identified rare and subtle clusters in overlapped regions even in the heterogeneous conditions (Song et al. 2021).

1.5 Aim of the Thesis

The idea of quantitatively analyzing the cells with Lensless Holographic Microscopy is an important area to focus on when the simplicity of building setup is considered. Traditionally, respective holographic images are selected either by labeling or visual confirmation one by one. This process is highly human-based and it limits the generalization capacity to be used in different applications. On the other hand, these holo-

graphic images are rich in context due to the superposition of objects and reference waves. Therefore, it can be used in neural training directly. Nevertheless, the inner mechanism of neural training is hard to understand and it is prone to provide wrong results. Therefore, an alternative method to quantify these images from reconstructed phase images becomes a necessary step for the quantified results.

Throughout the thesis, the main emphasis will be based upon using an effective, easy-to-use, and low-cost method for the detection and quantification of the cancer cells with lensless holographic microscopy setup. By mimicking the white blood cells with U937 monocyte cells and using MDA-MB-231-MB-231 human breast cancer carcinoma cells, it is shown that promising results can be achieved while differentiating these cells that may be used for the diagnosis of cancer. For this purpose, a lensless digital inline holographic microscopy setup is used to obtain quantitative phase images. Then, these label-free images are analyzed to create a differentiation model for the effective separation of cancer cells from monocyte counterparts. The proposed label-free quantitative analysis model is used to increase the efficiency of deep learning models. Also, a conditional image-to-image translation model is employed to lessen the burden of the computing step. This study has enabled a potential way for differentiating cells, as well as can be implemented to other cell analysis model.

CHAPTER 2

MATERIALS AND METHODS

2.1 Materials

2.1.1 Optical Setup

In the performed study, the partially coherent multi-color light-emitting diode (LED Engin-897-LZ400MA00) was used to obtain images from USAF 1951 test target to understand the optimal resolution (Newport, HIGHRES-2). By obtaining the images from different channels of LED, the effect of wavelength on the resolution is investigated. Also, for spatially filtering the partially coherent light, mounted precision pinholes of Edmund Optics with different diameter sizes are used. During this step, 50 (Edmund Optics, 56-282), 100 (Edmund Optics, 56-283), 200 (Edmund Optics, 56-284), and 500 (Edmund Optics, 56-287) μm pinhole sizes are used to show the effect on the resolution. Throughout the experiment, the pinhole to object distances is changed from 7.5 to 10 cm and 12.5 cm (z1). For the acquisition of holograms, the CMOS sensor of a 4K, 13 MP Camera Board (See3CAM-CU135 - eCon Camera Solutions) is used with the integrated camera sensor of AR1335 CMOS Sensor (On-Semiconductor 13 Mp CMOS Sensor) with 1.1 μm pixel size and backside illumination to decrease the incoming signal to noise ratio. The outer shelf of the proposed system and light source-pinhole grab rail is 3D printed from a 3D-Printer (Ultimaker 2+ Connect). The optical setup with 3D printed PLA shelf is given in the Figure 2.1.a, representative sketch is given in the Figure 2.1.b and illumination system components are given in the Figure 2.1.c.

2.1.2 Data Acquisition

To understand how cells can be analyzed with neural network models in holographic image datasets; classification, and object detection models are used to differentiate cells. Additionally, cellular image transformation is used to lessen the burden of computational steps. For these purposes, images taken from MDA-MB-231 and U937 cells are used to

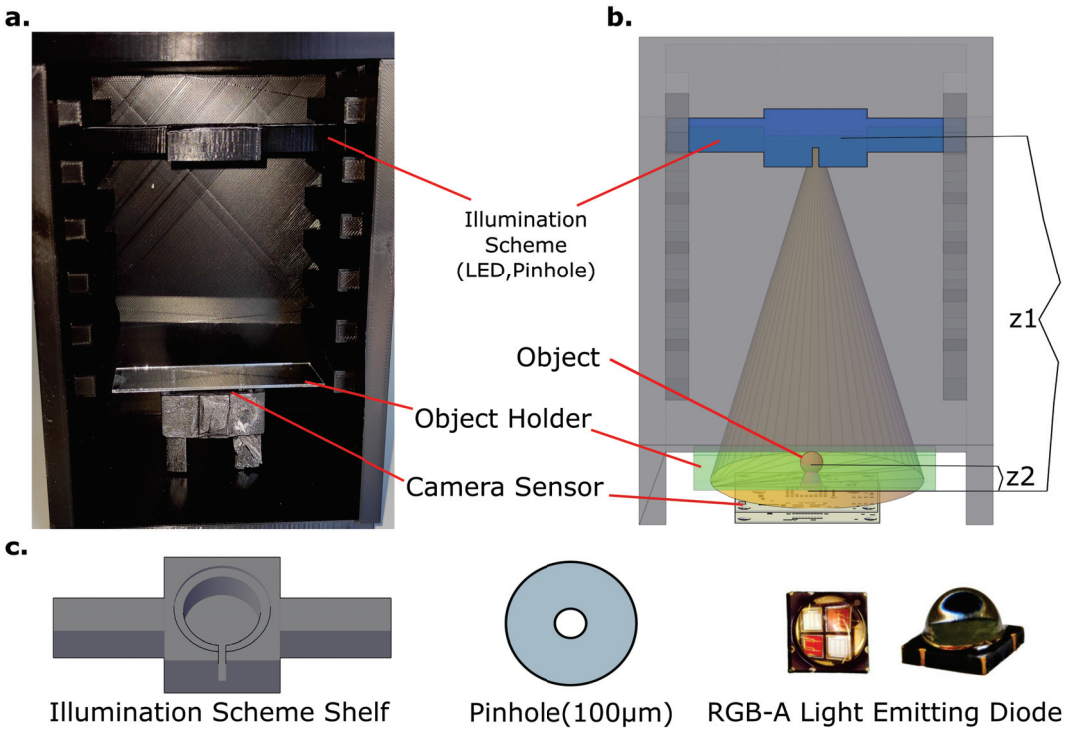

Figure 2.1: Optical Setup. a. 3D printed shelf. b. Representative sketch showing the components with distance values. c. Components of illumination scheme

feed deep learning models. During the experiments, U937 cells (Human monocyte, ATCC) are cultured with RPMI 1640 suspension medium and MDA-MB-231 cells (Breast Cancer cells, ATCC) are cultured with DMEM solution. MDA-MB-231 cells are cultured within 4 days of intervals and U937 cells have been cultured with 3 days of passage intervals. After the incubation step, they were diluted with DI water to become approximately $5 * 10^5$ cells per ml. The viability of cells is validated with Tryphan blue solution in hemacytometer as being 92% for MDA-MB-231 and 95% for U937. All images are captured with lossless 24 bit BMP format using 500 ms exposure time.

For creating the dataset from acquired holograms of each cell, 40 respective images are obtained through scanning the microfluidic channels. The microfluidic channel structure is composed of combining two microscopic slides with double side adhesive tape to create $50\mu m$ height channel is given in the Figure 2.2.a. The inlets are outlets are fixed with a PDMS (SYLGARD™ 184 Silicone Elastomer Kit). In order to clean up the glass slides, a piranha solution is used. The sectional view of the captured holograms' is given in the Figure 2.2.b with a microfluidic channel image contains the MDA-MB-231 cells.

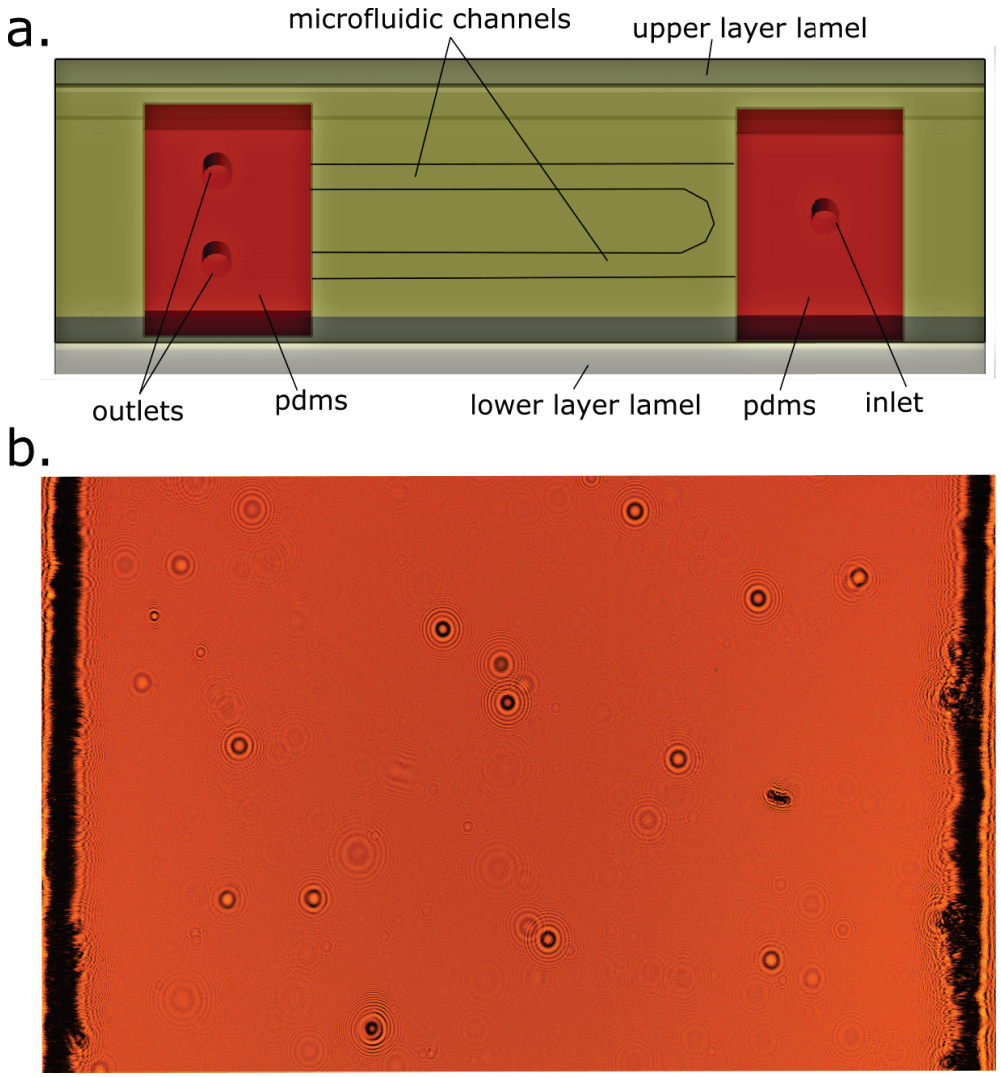

Figure 2.2: Hologram recording process. a. Microfluidic chip. b. Captured holographic image

2.2 Methods

2.2.1 Lensless Holographic Microscopy

2.2.1.1 Hologram Formation

In the application of Lensless Digital Inline Holographic Microscopy (LDIHM), the light source can be either coherent (Zhang et al. 2018) or partially-coherent (Repetto,

Piano, and Pontiggia 2004). Since coherent light sources such as lasers are expensive and induce coherency-based noises, their usage requires an extra alignment step with an expensive setup for Lensless Digital Inline Holographic Microscopy. On the other hand, it is shown that incoherent illumination can increase the signal-to-noise ratio compared to coherent illumination (Gorocs and Ozcan 2013). By inducing a well-aligned distance from the pinhole to object and object to hologram distance, required coherency can be maintained with partially coherent light sources. Thus, for the partially coherent illumination, a light-emitting diode (LED) is used with a pinhole to spatially filter the system to remove the high-frequency components. To obtain enough spatial coherency on the object plane, the associated pinhole diameter size needs to be greater 100λ up to 200λ. This condition also helps us to decrease the interference within multiple cells as well as decrease the speckle noise associated with the coherency of light source (Mudanyali et al. 2010).

In addition to the spatial filtering by a pinhole required coherency on object plane condition depends on multiple parameters (Wu et al. 2018). One of the dependence is about the spatial coherency diameter ($D_{spa-coh}$) to full-fill enough coherency on the sample plane is given in the Eq. 2.1. It needs to be greater than the cell's diameter and most of the time, it is satisfied with a large pinhole size within the visible light region.

$$D_{spa-coh} = \frac{\lambda * z1}{D} \tag{2.1}$$

where z1 is the distance between pinhole to object plane and D is the diameter of the object.

The temporal coherence length of the system ($D_{temp-coh}$) is another limiting factor that depends on the light source characteristics which is given in the Eq. 2.2;

$$D_{temp-coh} = \frac{2 * \ln 2}{\pi} * \frac{\lambda^2}{n * \Delta\lambda} \tag{2.2}$$

where λ is the incoming light wavelength, $\Delta\lambda$ is the change of spectral bandwidth of the light source and n is the refractive index of the medium.

Illuminated objects have different refractive index values within the different points of objects. Therefore, the cell plane acts as a source of object waves and interact with reference waves to form a differentiated pattern on the hologram plane. To avoid any interference between these interference patterns, their projected effective width needs to be smaller than the pixel size of the camera sensor to lessen the effect of incoherency. The effective width of each point scattered from the object on the sensor plane is called

d. (d= $D * \frac{z_2}{z_1}$). This can be easily satisfied with a scaling factor of the system (M = $\frac{z_1}{z_2}$) that is associated with a proportion of pinhole to object distance (z1) to object to hologram plane distance(z2). It needs to be much larger than 1 (M>>1) to satisfy the coherency condition. In typical setups, this ratio is around 40 to 100. By maintaining such a coherency, it is shown that each cell can be captured coherently without affecting their spatial features(Mudanyali et al. 2010). This property of the inline systematic makes it possible to treat micron-sized cross-sections of objects as illuminated with a coherent plane wave. But most importantly, since each cell can be treated differently from the entire CMOS sensor plane, the efficient field of view (FOV) is now increased to 20 mm^2 to make the system quite usable for point-of-care applications (Greenbaum et al. 2012).

Previous studies on the hologram recording step are generally takes the advantage of the large pinhole to object plane distance. Also, by taking the smallest object to hologram plane distance (z2), unit magnification with a large field of view advantage is used in these studies (Mudanyali et al. 2010) Easy alignment of LDIHM systems makes it possible to be used with many modalities. The resolution achieved in the LDIHM system is based upon many factors. The most important limiting factors are wavelength, the bandwidth of the light source, pinhole diameter, the distance between the pinhole to the object plane, the distance between the object to the hologram plane, and the pixel size of the camera sensor. To understand the effect of these parameters on the resolution; different LED light sources are used, the diameter of the pinhole is changed, and used different pinhole-to-object distances are used to find the maximum achievable resolution.

In LDIHM, two main systematic are used while forming the hologram. Depending on the distance between pinhole to object plane denoted as z1 either the spherical or plane wave formation is used. In the plane wave systematic which is given in the Figure 2.3.a, an object is positioned very close to the hologram plane (z2) and light propagates from pinhole to object plane (z1) to gain coherency so that it can be treated as a plane wave. In the spherical wave systematic that is given in the Figure 2.3.b, an object is positioned very close to the light source or pinhole to directly interact with light and propagated towards the hologram plane by the superposition of the object and reference waves. The main components of both systems are given in the Figure 2.3.c.

Throughout this thesis, the plane wave systematic are used to obtain coherency and a large field of view. Incident plane wave $exp(k_x.x + k_y.y + k_z.z)$ on the object plane wave vector components with (x,y,0) coordinates described as $U_{inc}(x, y) = 1$. If there is no object exists or either the absorption or the phase is considered to be 0, then the transmission function becomes t(x, y) = 1. After the light passes from object, it is described as $U_{exit}(x, y) = t_f(x, y)$. Then, the resultant exit wavefront distribution is given in the Eq 2.3;

$$U_{exit}(x, y) = U_{inc}(x, y).t(x, y) = U_{inc} + U_{inc}.t_f(x, y) \tag{2.3}$$

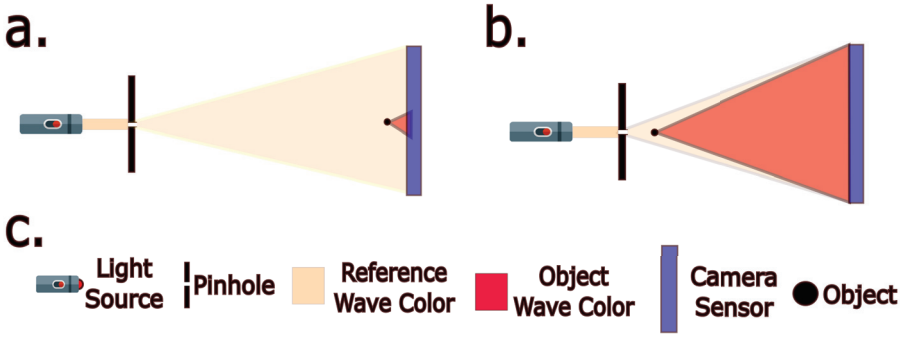

Figure 2.3: Hologram formation in lensless holography. a. Plane wave, b. Spherical wave. c. Optical components of these systems

where $U_{inc}(x, y)$ is the incoming wave, t(x,y) is transmission function and $U_{exit}(x, y)$ is the wavefield after propagating with object.

The acquired object wave propagated from object plane (x,y) to detector plane (X,Y) with Fresnel-Kirchoff diffraction formula that is given in the Eq 2.4;

$$U_{holo}(X, Y) = \frac{-i}{\lambda} \int \int U_{exit}(x, y).t_f(x, y) \frac{exp(ik|\vec{r} - \vec{R}|)}{|\vec{r} - \vec{R}|} dxdy \tag{2.4}$$

where λ is the wavelength of the source, and $U_{holo}(X, Y)$ is the intensity of the recorded hologram as a result of propagation. In the equation, transformation term $|\vec{r} - \vec{R}| = \sqrt{((x - X)^2 + (y - Y)^2 + (z)^2}$ is used with perturbed transmission function where $\vec{r}$ represents object plane components (x,y,z), $\vec{R}$ represents hologram plane components (X,Y,Z).

2.2.1.2 Numerical Reconstruction and Phase Unwrapping

In the LDIHM systematic, both the reference and object wave comes from the same direction. In the equation, the first term represents the reference wave and the second one is the object wave which is too small that can be disregarded (Latychevskaia and Fink 2007). The third and fourth terms represent the conjugate twin image terms of the twin-image artifact. Therefore, the captured wave-field consists of the superposition of two waves that is given in the Eq 2.5:

$$|U(X,Y)|^2 = |R(X,Y)|^2 + |O(X,Y)|^2 + R^*(X,Y).O(X,Y) + R(X,Y).O^*(X,Y) \quad (2.5)$$

where the resultant hologram pattern intensity is described as $|U(X,Y)|^2$. U(X,Y) refers to captured hologram amplitude, O(X,Y) refers to object wave, and R(X,Y) refers to reference wave.

In the hologram intensity equation, the hologram represents the complex wavefield information of an object in the recording plane as an intensity measurement. This intensity measurement has complex numbers which are specific to objects' properties. At this point, the camera sensor has a similar property to mimic concave lens, in both directions, an image is formed. When we back-propagate the intensity pattern with Fourier Transform, two complex conjugate terms are overlaid due to the Hermitian property of Fourier space to form twin-image phenomena (Popescu 2019). The one that remained in the backside of the hologram is called a real object and the one obtained during reconstruction is called a twin image which is positioned between the object plane and hologram plane. Actually, at this point, some views state that the real image remains on the side of the pinhole (Latychevskaia and Fink 2015). But when the image is considered to be formed on the hologram plane which refers to 0th order interference pattern, +1 order real image needs to be z2 distance behind the hologram. Nevertheless, these overlapped complex conjugate terms are the main reason for lost phase information which limits the accurate shape reconstruction of objects. Therefore, in addition to the reconstruction step, an extra phase retrieval step needs to be performed to obtain accurate real image terms. The details of the phase retrieval process are explained in the phase retrieval section later, in this section, the direct numerical reconstruction step will be evaluated.

Main idea of the reconstruction step is to find an approximate solution starting from the hologram plane (X,Y) to propagate up to the object plane (x,y) utilizing numerical solution by propagating distance z2. This propagating distance represents an approximate solution for a distance between the individual cell to the recorded hologram. This numerical solution starts from the assumption of the whole cells are illuminated with a plane wave with enough coherency due to the large M ($\frac{z1}{z2}$) number. In this assumption, the plane wave is taking into consideration because of the large M value. Therefore, no approximation is needed with a small z distance to use the angular spectrum method (ASM). The captured hologram can be directly back-propagated to a real or twin image plane by ASM. Systematic representation of the real and twin image with reconstruction steps is illustrated in the Figure 2.4.a with corresponding distance values for the reconstruction

from z2 to -z2 is given in the Figure 2.4.b.

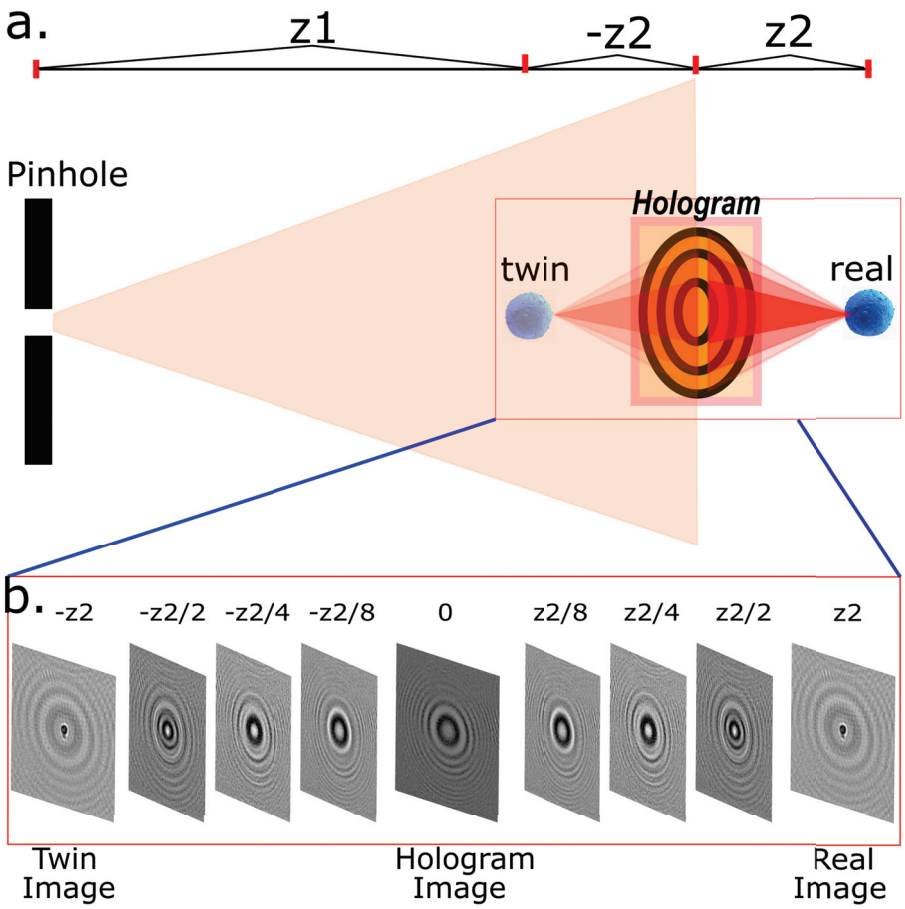

Figure 2.4: Reconstruction step with conjugate twin image terms

Angular spectrum method is based upon taking the wave propagation as a propagation of its spectrum. Therefore, it uses no approximation (Goodman 1968). The analysis was performed by taking the Fourier transform of the recorded hologram and propagating it with a free space transfer function up to the object plane. Therefore, as an initial step wave vector components are converted into Fourier domain with the Eq 2.6;

$$\vec{k} = \frac{2\pi}{\lambda}(cos\varphi.sin\theta, sin\varphi.sin\theta, cos\theta) \tag{2.6}$$

where the term (u,v) represent the fourier domain coordinates. The respective transformations for u coordinate is $cos\varphi.sin\theta = \lambda u$ and transformation for v coordinate is $sin\varphi.sin\theta = \lambda v$. In these transformations, $(\lambda u, \lambda v)$ denotes the wavevector components which needs to full-fill the frequency requirement of the possible range assumption to treat

system as performed in classical resolution limit stated by the Eq 2.7:

$$(\lambda u)^2 + (\lambda v)^2 \leq 1 \tag{2.7}$$

Then, the obtained exit wave t(x,y) is propagated to the detector plane by the following transformation of the Eq 2.8;

$$U_{detector}(X,Y) = FT^{-1}[FT(t(x,y)).exp(\frac{2\pi iz}{\lambda}\sqrt{1-(\lambda u)^2-(\lambda v)^2})] \tag{2.8}$$

where z is the distance between the object to the hologram plane that is taken as z2 in our study.

In the final reconstruction step, the obtained term is back-propagated to the object plane by the free space transfer function that is given in the Eq 2.9:

$$U(x,y) = FT^{-1}[FT(U_{detector}(X,Y)).exp(-\frac{2\pi iz}{\lambda}\sqrt{1-(\lambda u)^2-(\lambda v)^2})] \tag{2.9}$$

where $U_{detector}(X,Y)$ is the captured complex valued intensity measurement.

In the final step, in the object plane, the complex-valued Fourier transformed term is separated into amplitude and phase spatial components with absolute and arctan functions (Delikoyun et al. 2021b).

Another problem of the reconstructed object is about the discontinuity of phase radian values that are placed between $-\pi$ to π due to frequency spectrum restrictions while taking Fourier transform. The phase shift obtained more than the modulus of $-\pi$ to π value between two pixels goes into a replacement from to start from the other end of the modulus. So, the actual phase shift is wrapped during this reconstruction step, and a correction function is required to regulate the continuity of the phase shift. Such a solution can be obtained with simple functions but the success associated with optimal phase shift depends on accurate calculations even in noisy conditions. This can be achieved by solving the transport of intensity equation by fast cosine transform (Zhao et al. 2018).

2.2.1.3 Iterative Phase Retrieval

The iterative retrieval methods are divided into two categories based upon the number of intensity measurements. In the single-shot retrieval, the hologram's only intensity measurements are taken with background constraints to reduce the number of unknowns. For the multi-shot retrieval, two or more intensity measurements are taken by inducing different acquisition conditions. Therefore, both methods find different applications areas.

In the single-shot retrieval methods, instead of taking multiple shot measurements, prior knowledge about the object is taken to induce as a source of constraint. As an initial point, the acquired hologram intensity is taken with an initial zero or random phase assumption. Before the reconstruction step, captured holograms are 4x bicubic interpolated. This step gives an extra advantage to smooth the edges and helps sub-cellular interpolated components to gain non-zero energy. Then, the obtained complex waveform is back-propagated to the object plane by equation 2.8 given in the previous section. This process is performed by multiplying wave patterns with a free space transfer function starting from the hologram plane up to the object plane. In the object plane, a constraint-based on the representative object shape is applied to filter this complex wave pattern. Then, the background normalization is performed by inducing object-free measurement by replacing the area outside the applied constraint. Then, the resulting complex waveform forward propagated to the hologram plane. In the hologram plane, the phase of the complex wavefront is preserved while the amplitude is replaced with initial intensity measurement. Therefore, an updated version of the initial hologram is acquired with an iteration step (Mudanyali et al. 2010). This iteration is performed multiple times up to converge conditions satisfied. The initial process is masking and interpolation of the corresponding cell is given in the Figure 2.5.a. In the second step, an iterative Gerchberg-Saxton algorithm is used to iteratively retrieve the lost phase information. In each iteration, the phase value is updated and finally, it gains a convergence point where it is no longer updated. After the final iteration step, obtained resultant complex wavefront back-propagated to the object plane with inverse Fourier transform to separate amplitude and phase components is given in the Figure 2.5.b.

To apply a multi-shot process to retrieve phase information, the process described in the work of Zhang et al. is applied (Zhang et al. 2018). The proposed method uses a maskless process without background normalization steps to retrieve phase information accurately. Also, the main assumption is about the high similarity between obtained phase shift information to be able to replace the iteration at each object plane. The algorithm starts with initial random phase information and by taking the square root of intensity measurement. Obtained complex wavefront is propagated to object plane with λ_1 propagation. In the respective object plane, the obtained amplitude is updated

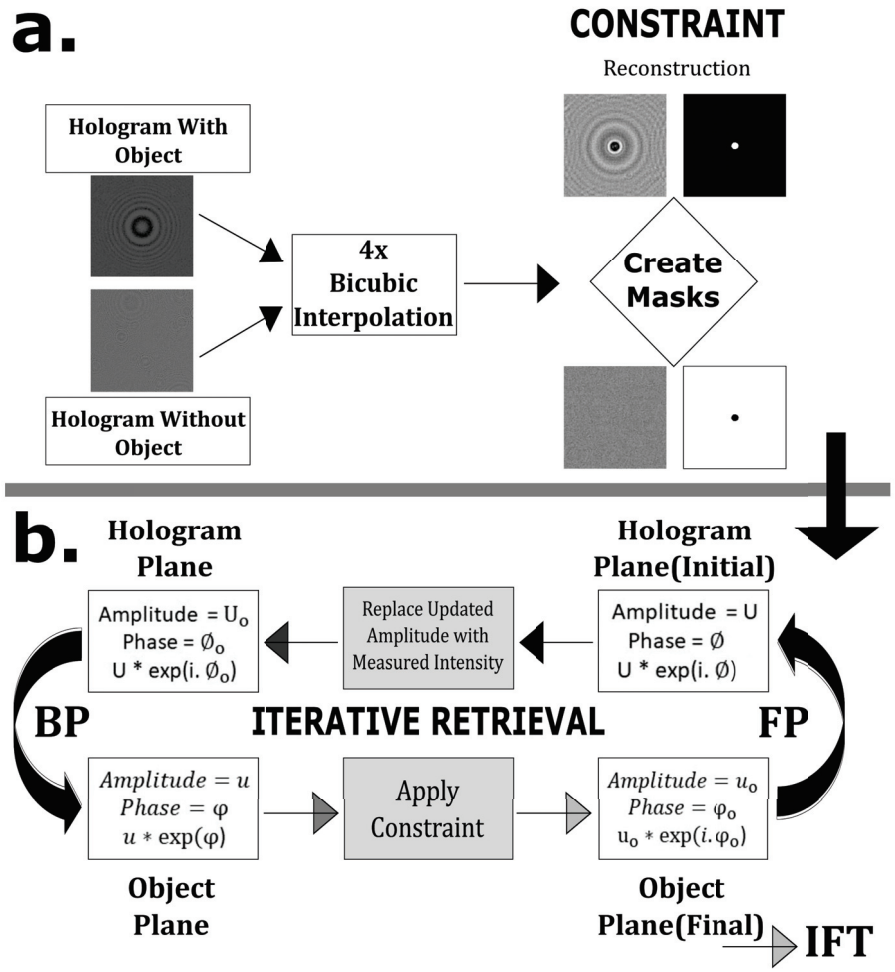

Figure 2.5: Single-shot phase retrieval systematic. a. Pre-processing and masking step. b. Iterative Gerchberg & Saxton phase retrieval algorithm

with the amplitude value of the second hologram. Within this step, phase information is also replaced with the updated object plane phase value with the equation of $\phi_{o2} = \phi_{o1} * \frac{\lambda_1}{\lambda_2}$. Next, the obtained wavefront is back-propagated to the hologram plane with λ_2 propagation. At the respective plane, phase information is preserved but this time, the retrieved amplitude is replaced with second wavelengths' intensity measurement. Then, the complex wavefunction is again propagated to the object plane with λ_2 propagation. This time, same process is applied to update amplitude to object plane 1 and phase information is replaced with $\phi_{o1} = \phi_{o2} * \frac{\lambda_2}{\lambda_1}$. This time, wavefunction back-propagated to object plane with λ_1 propagation. As a final step, obtained amplitude value is replaced with initial intensity measurement while keeping the updated phase information. In this way, an iteration is completed and it is repeated until the convergence of obtained phase information is achieved. Typically, it takes 20 iterations to reach desired values. The workflow for the multi-wavelength phase retrieval method is given in the Figure 2.6.

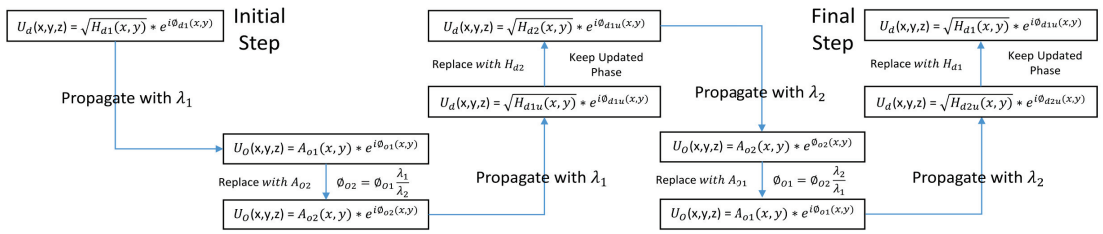

Figure 2.6: Multi-wavelength phase retrieval process

2.2.2 Conditional-GAN for Cellular Image Transformation

After the first effective implementations of GAN models, Mirza et al. introduced another effective way to generate images by applying initial conditions on generated data (Mirza and Osindero 2014). These additional inputs could be anything related to the data such as a particular class value or name. The generative model takes this input to generate conditional predictive results. Also, the discriminator model again has conditional acceptance to update its guess. Such models are widely used in the image-to-image translation models such as photo colorization tasks (Nazeri, Ng, and Ebrahimi 2018). Later on, a generalized version of conditional generative adversarial network (cGAN) models are introduced with pix2pix model to learn the loss during input to output mapping. This mapping-based approach makes it possible to easily build up loss function even in very different conditions (Isola et al. 2017). The model used in this transformation is given in the Figure 2.7.

As an initial study, reconstructed amplitude images are converted to reconstructed phase images to directly obtain arctan counterparts. In the second model, the obtained reconstructed phase images are used to convert into twin-image artifact-free counterparts that come from the single-shot iterative retrieval steps. In this way, instead of the long processing time of the one-to-one phase retrieval step, the required computation time could be eliminated by directly generating the image results with the previously trained cGAN model weights. Two models are used different datasets in the pix2pix training stage with a crop size of 256x256. During this training step, an open-source platform of ZeroCostDL4Mic (Chamier et al. 2021) is used with the model of pix2pix image to image translation model (Isola et al. 2017). In the first dataset, amplitude to phase conversion is used with directly reconstructed images. The model is trained with 1395 images. To understand the training efficiency of the model, 5 images are used to obtain mean Structural Similarity Index Matrix values (mSSIM) of images. These selected 5 images have similar intensity profiles. The mSSIM metric uses an 11 pixels window with surrounding structural similarity matrices to obtain a value between 0 to 1. It evaluates the

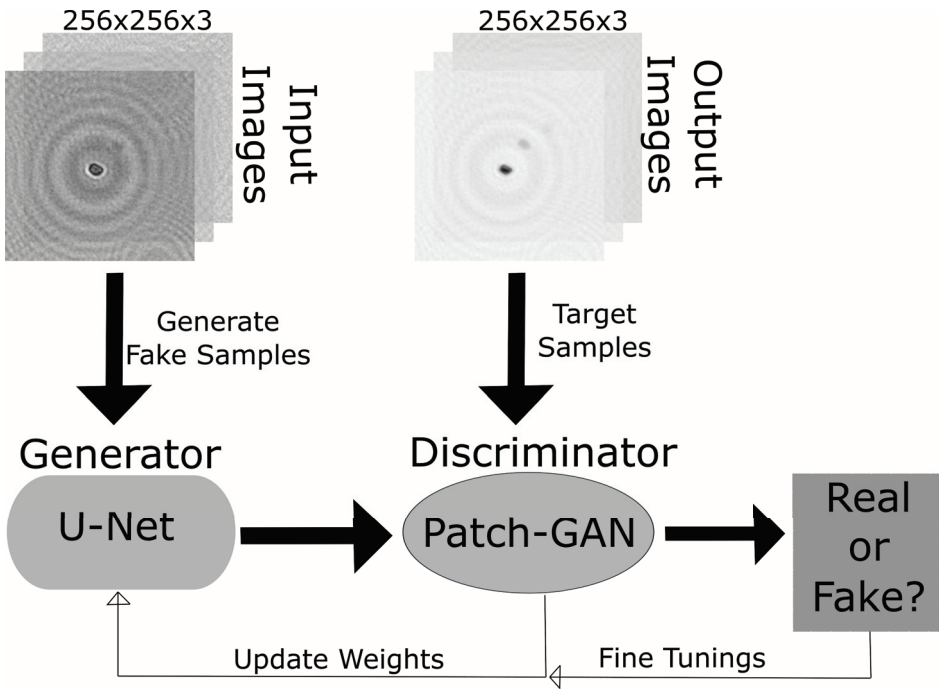

Figure 2.7: pix2pix conditional-GAN systematic

normalized similarity between two images and a metric close to 1 represents the perfect match. During the training step, TESLA P100-PCI-E GPU is trained in 50 epochs with a patch size of 256 that is the minimal crop size. A batch size of 1 is used and the initial learning rate is set to be 0.0002 with Vanilla GAN loss function. Training takes 52 min 37 seconds.

In the second model, from directly reconstructed phase images to phase retrieved counterparts are used to obtain twin-image free images from the cGAN model. The purpose of this image-to-image transformation is to lessen the burden of computing for the iterative phase retrieval step. In this model, 1506 images are used for training and tested with 5 images. Training is performed on TESLA P100-PCI-E GPU with 200 epochs. The patch size of 256 is selected that is the minimal crop size. A batch size of 1 is used and the initial learning rate is set to be 0.0002 with Vanilla GAN loss function. Training takes 3 hours 47 min 9 seconds.

2.2.3 Classification and Detection of Cells

Convolutional neural network(CNN) models use the same structure of human neurons to transmit information from input to output to characterize its function. In such a model, the object matrix goes through a set of mathematical operations in each layer (Alzubaidi et al. 2021). In the initial layers, the model uses a set of filters to scan the

input matrix to create a set of feature maps. This process uses a convolution operation to extract the features from different parts of the object. The convolution process takes each pixel value within blocks to apply matrix multiplication to each pixel individually. By applying different filters, corresponding feature maps are obtained. In the following layer, an activation function is used to increase non-linearity between obtained features. An activation function is used to set a bridge between the incoming layer to transfer obtained information to the next layer by adding some non-linearity. The most common activation functions are Sigmoid and Rectified Linear Unit(ReLU) that have different functions specific to the target. In the next layer, either another convolutional layer could be used or a pooling layer can be used to decrease the number of parameters. This process is achieved by taking average or maximum values within certain blocks and trajecting the values of whole matrices to the next layer. The next layer is again another convolutional layer to collect specific features. This process is repeated many times to decrease the number of parameters and also extract features into narrower outputs. In the final layer, a fully connected takes the input of each previous layer to create a probability between 0 and 1 to define how well the model defined the accurate or desired result. Depend on the obtained results, a backpropagation is applied until convergence is achieved to keep continue updating the initial weights and parameters. In a typical CNN structure, the number of applied layers could go from tens to hundreds. But deepening the layer sacrifice the amount of time for the computation. Also, the number of weights updated during training is different from one structure to another.

After the first effective usage of CNN models, the deeper structure of models starts to be problematic when back-propagated gradients are being quite small. The main solutions in this area come with the introduction of Residual Network Models(ResNet). By identifying a shortcut connection between multiple layers, it is possible to use deeper models without sacrificing the performance of a model. During their study, He et al. (He et al. 2016) proposed an identity function to link between several layers to be able to optimize deeper networks in much easier ways. After their first findings, they showed how to obtain better performance with 1001 layer deep neural networks (Kaiming He and Sun 2016).

Here, as a preliminary study to understand how a basic transfer learning-based Resnet model can differentiate cells, 954 images are cropped from each cell with a cropping size of 200x200. These crops are selected randomly through the channels. Train:Val:Test splits ratio set to become 754:100:100. In this training; train, validation, and test datasets are put into different folders. This selection is performed randomly instead of in the cross-validation step. Because the respective test dataset is compared with the final quantitative results. Starting from the Transfer Learning models, different Resnet architectures (Resnet18, Resnet 34, Resnet 50, Resnet 152) are used to train created cells datasets. As a final model, the Resnet-34 structure is selected when the time and

performance are considered. A batch size of 32 is used in this training. The initial learning rate set to be 0.001, momentum is taken as 0.9. As an optimizer, SGD model is used. During training, Google Colabs' TESLA P100-PCI-E GPU is used and it takes 286 seconds to process 50 epochs. The traditional structure of CNN and replaced Resnet shortcut model is given in the Figure 2.8.a. The CNN structure based on the transfer learning model with the corresponding layers and filters is given in the Figure 2.8.b.

a.

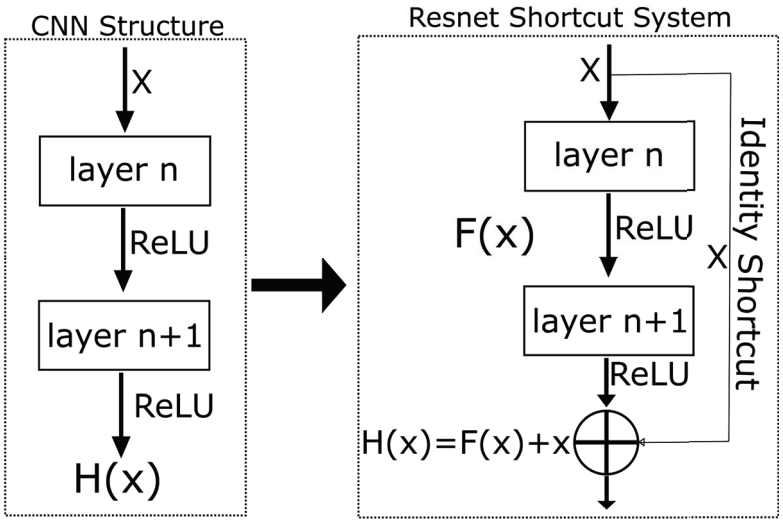

b.

Layer Name	Resnet-34 Model Structure	Output Size
conv1	7x7, 64, Stride 2	112x112
pool1	3x3, max poll, stride 2	112x112
conv2_x	$\left[\frac{3x3,64}{3x3,64}\right]x3$	56x56
conv3_x	$\left[\frac{3x3,128}{3x3,128}\right]x4$	28x28
conv4_x	$\left[\frac{3x3,256}{3x3,256}\right]x6$	14x14
conv5_x	$\left[\frac{3x3,512}{3x3,512}\right]x3$	7x7
fully connected	average pool, 2d fc, softmax	1x1

Figure 2.8: Classification process. a. CNN and Resnet Shortcut System Comparison. b. Resnet 34 model

In the systematic of YOLO object detection algorithm, Each cell is processed individually throughout the model to predict corresponding position values(x,y) and image height-weight. Also, it gives a confidence score to interpret the probability of the object. Then, the results from each cell are taken together to form the final set of results by a non-max suppression model to eliminate the scores below a certain limit. In this way, the most probable object classes with efficient and fast results are achieved with the

proposed structure that is given in the Figure 2.9. One of the main successes of YOLO is coming from its capability to generalize models dependless on the object classes. With the achievements in this area, the last version of YOLOv5 with open-source codes has increased the usage with efficient results (Jocher et al. 2021).

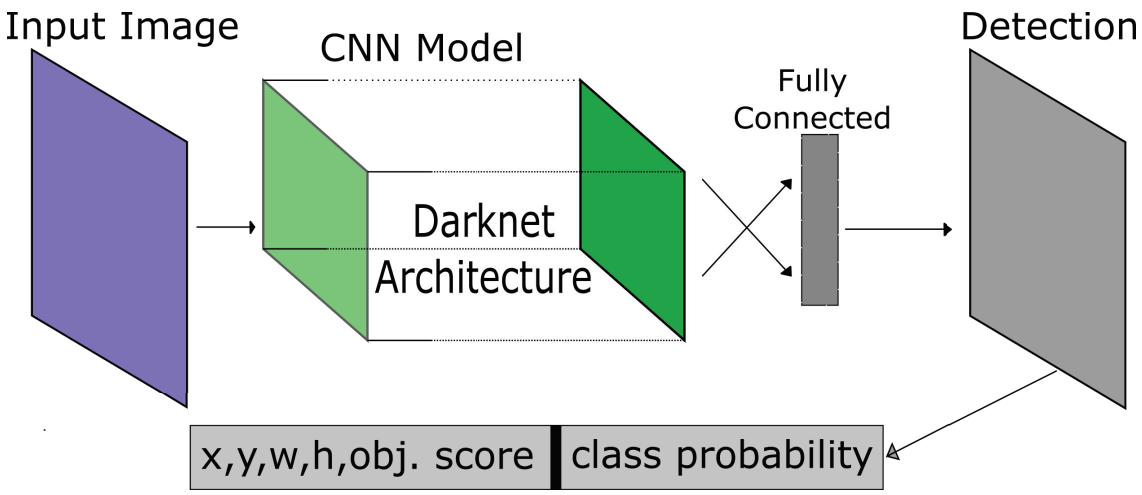

Figure 2.9: YOLO architecture

To process the object detection in the same cells dataset, the initial large field of view hologram images are cropped with a size of 2000x2000 pixels. A total of 162 images are used with the YOLOv5s model. Annotated label numbers for MDA-MB-231 and U937 are 1103 and 1252 respectively. In order to obtain a similar dataset with the classification part, overlapped cells are not labeled. Train:Val:Test ratio of 140:16:6 is used in the training. 2000 epoch is trained with TESLA P100-PCI-E GPU in 2.6 hours.

2.2.4 Quantification Method for Cells

In this analysis part, quantitative phase images of cells are used without any phase-retrieval step. Because the obtained holograms from microfluidic channels are not fixed during the experiments, they were sliding while taking the brightfield counterparts. Therefore, the accurate twin-image elimination by crosschecking with brightfield counterparts is not directly possible in the iterative phase retrieval step. Also, the fixing procedure can affect the object characteristics and structure of cells. Therefore, reconstructed phase images are used to provide approximate object shape and phase shift value to be used as a quantitative differentiation mechanism. This analysis step will enable us to quantify object

characteristics and provide more accurate results to differentiate cells when compared to holographic images. On the other hand, the proposed mechanism uses 4 steps to eliminate error-prone images based on the percentage error mechanism. Most of the eliminated images represent the dust particles, low-SNR ratio cells, cell assemblies, or dead cells. Therefore, it is important to take away them before putting them into quantified neural training models. In addition, the proposed method can be used to generalize for different objects and have a tendency to be performed in an automatized manner in future studies.

The proposed method is illustrated in the Figure 2.10.a. At this step, the analysis is performed within 4 steps by the direct interruption. In each step, percentage error-based elimination is used to disregard corresponding images given in the Figure 2.10.b. Initially, 954 hologram images are reconstructed to obtain phase images from MDA-MB-231 and U937 cells. In each elimination step, the initial mean value is calculated and below 50% percent value images are disregarded for the next step. Initial elimination is based upon the quantitative phase shift value (radian). Then, the phase images are binary masked. In the third and last step, perimeter and circularity values are retrieved and 50% percent error images are taken to eliminate corresponding holographic images.

The first differentiation method is based upon the phase shift value(radian) of the object. Even though some proportion of phase information is lost during the reconstruction step, it still contains valuable phase shift information in terms of radian. This differentiation mechanism is mainly based upon object thickness as well as related to the inner property of an object. Instead of normalizing the obtained phase values to represent intensity images, they are directly taken from back-propagated values. Therefore, it provides strong information specific to the object differences. The percentage error of each cell is calculated by the Eq. 2.10:

$$\delta = \left|\frac{\phi_{actual} - \phi_{mean}}{\phi_{mean}}\right| * 100 \tag{2.10}$$

where ϕ_{actual} represents the obtained phase shift value, ϕ_{mean} represents the mean phase shift of the corresponding cells and δ is the obtained percentage error value.

Second step is performed by creating the binary masks of remained cells that are 804 for the MDA-MB-231 cells and 771 for the U937 cells. Reconstructed phase images are used in this step with an open-source Ilastik program to create binary masks (Berg et al. 2019). In the corresponding software, pixel classification model is used to train several cells initially to create a general model. Then, the area inside the object is taken to create binary masked images with a pixel-based method and generalized into the batch process to obtain binary masks for the whole image. During this step, due to the very low-SNR ratio, some of the binary masks do not represent any continuous shape structure.

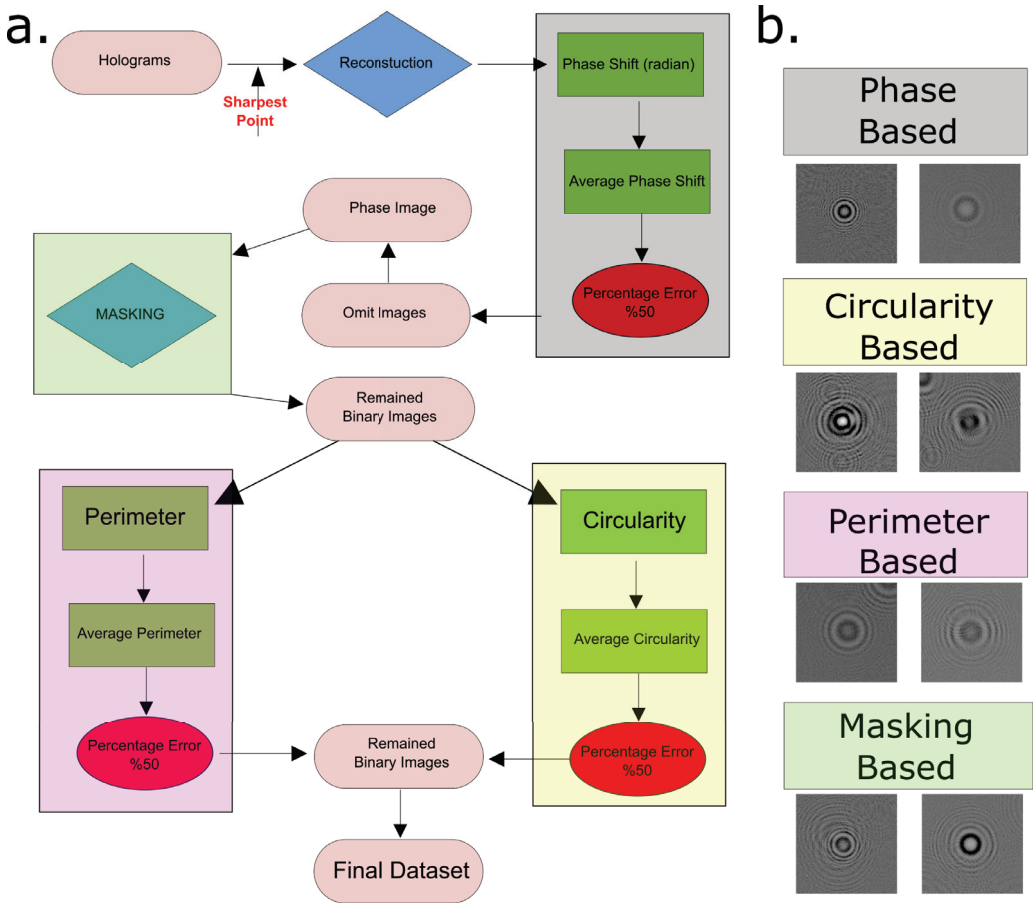

Figure 2.10: Quantitative analysis step. a. Elimination model. b. Example of eliminated cells with corresponding steps

Their discontinuity preventing the calculation of perimeter or circularity value when the respective boundary function is applied to the discontinuous shape structures. Thus, some of the cells are disregarded in the binary mask step.

In the third step, the perimeter value of the object is obtained with Matlab's boundary threshold function. This function takes the input binary image and encloses the inner boundaries by filling the holes. Then, the differential change within the binary mask is calculated to find the boundary of objects. Since the inner mask in a binary image have value of 1 and outer layers have value of 0, the boundary value is calculated in terms of a number of pixel and differential value. This obtained value represents the perimeter of the obtained mask. In addition, the area of the object is calculated in this step after the filling procedure.

In the fourth step, the circularity of cells is calculated with the obtained values from the third step. Perimeter and area values are used with the Eq. 2.11 to find the circularity values (Bottema 2020).

$$Circularity = \frac{4 * \pi * area}{perimeter^2}; \tag{2.11}$$

CHAPTER 3

RESULTS AND DISCUSSION

3.1 Analysis of Lensless Holographic Microscopy

3.1.1 Optimization

At the first step of the optimization, pinhole to object distances are changed (z1) starting from 7.5 cm to 12.5 cm with 2.5 cm increments. At each height, the pinhole size of 50, 100, 200, and 500 μm pinholes are used. In addition to changing the pinhole sizes, different color channels of RGB-A LED are used to understand the effect of wavelength. Blue (460 nm), Green (525 nm), Amber (590 nm), and Red (621 nm) channels give different resolution values with associated height and pinhole sizes. Their obtained resolution values are given in the Figure 3.1.

RGB-A LED

Pinhole Diameter	Blue Channel 460 nm			Green Channel 520 nm			Amber Channel 590 nm			Red Channel 620 nm		
	z1 Distance			z1 Distance			z1 Distance			z1 Distance		
	7.5 cm	10 cm	12.5 cm	7.5 cm	10 cm	12.5 cm	7.5 cm	10 cm	12.5 cm	7.5 cm	10 cm	12.5 cm
50 µm	1.95 µm	2.19 µm	2.46 µm	2.19 µm	2.76 µm	3.1 µm	2.19 µm	1.95 µm	3.1 µm	2.19 µm	2.76 µm	2.76 µm
100 µm	2.46 µm	2.46 µm	2.19 µm	2.46 µm	2.76 µm	3.1 µm	1.95 µm	1.95 µm	2.76 µm	2.46 µm	2.76 µm	2.76 µm
200 µm	2.46 µm	2.46 µm	2.46 µm	2.76 µm	2.76 µm	2.76 µm	2.19 µm	2.19 µm	2.46 µm	2.76 µm	3.1 µm	2.76 µm
500 um	3.1 µm	2.76 µm	2.76 µm	3.1 µm	3.48 µm	3.1 µm	2.76 µm	2.75 µm	2.76 µm	3.48 µm	3.48 µm	3.1 µm

Figure 3.1: Resolution values for different wavelengths of the RGB-A LED

By looking at the obtained resolution values, it can be seen that maximum achievable resolution is obtained from the amber channel(590 nm) of the RGB-A LED. Although closer results are achieved from the blue channel, the general values of amber channels have better resolutions. The minimal distance between the object to the hologram plane (z2) is found to be 0.86 mm as an approximate value from the numerical reconstruction step that is specific to USAF 1951 test target. The optimal pinhole to object distance (z1) is taken as 10 cm due to obtained higher resolution values compared to other channel values. Also, the optimal pinhole size is taken as $100\mu m$ due to the higher intensity signal.

The best resolution achieved through these optimization steps is 1.95 μm. This value is determined directly from the reconstructed amplitude image of the USAF-1951 Test Target. To characterize the obtained resolution power, three lines from vertical and horizontal directions need to be resolved, in other words, we need to see 3 peaks corresponding to the same positions with similar increments throughout the line. Also, the line profile taken from cross-section points needs to be 5 times the resolution power of the system. The reconstructed USAF 1951 test target is given in the Figure 3.2.a and zoomed version is the Figure 3.2.b with corresponding vertical and horizontal intensity cross-sections are given in the Figure 3.2.c.

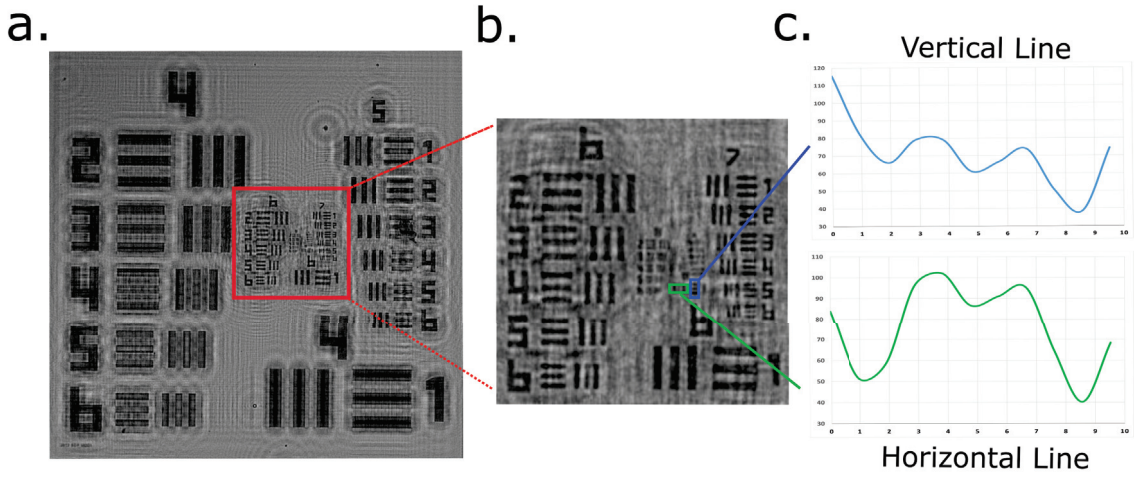

Figure 3.2: Optimal resolution. a. Reconstructed 1951 test target. b. Zoomed version of test target. c. Quantification line profiles of group 8 element 1

The small alignment differences during the experiments may have been affected the obtained resolutions. Since the LDIHM setup has a small tendency to be affected by the alignment step due to its small distance between light source and pinhole, the effect of this alignment step has been ignored. From the experimental resolution findings, as a generalization, it can be stated that shorter wavelength light sources can be used with smaller pinhole to object sizes and longer-wavelength light sources tend to obtain coherency with a larger z1 value. Changing the pinhole size affected the obtained light flux from the system. No clear differences were obtained between 50,100 and 200 μm pinholes. The shorter bandwidth value of the light source is an important characteristic to obtain the required coherency. In addition to the light source and systematic of the setup, camera sensor response to different wavelength values is found to be quite important. Since the optimal resolution values are found from the amber channel of LED, it states that the

red channel of the camera sensor has good response at 590 nm wavelength. Therefore, reconstruction steps are performed with red channel values. The reconstruction step of acquired holograms is performed based on the sharpest value manner to automatically found the optimal object to hologram distance z2. At this point, as an additional parameter, approximated object to hologram distance value is set to become in a certain interval. In this way, progress speed is increased and the error rate is reduced. All the reconstruction steps are performed with angular spectrum methods. Obtained unwrapped phase images are used in the rest of the thesis.

3.1.2 Numerical Reconstruction and Phase Unwrapping

The numerically back-propagated images from the direct reconstruction step have a similar structure to the actual shape of the object. Captured hologram, corresponding reconstructed amplitude and phase images, and obtained phase shift value are given in the Figure 3.3.a,b,c,d respectively.

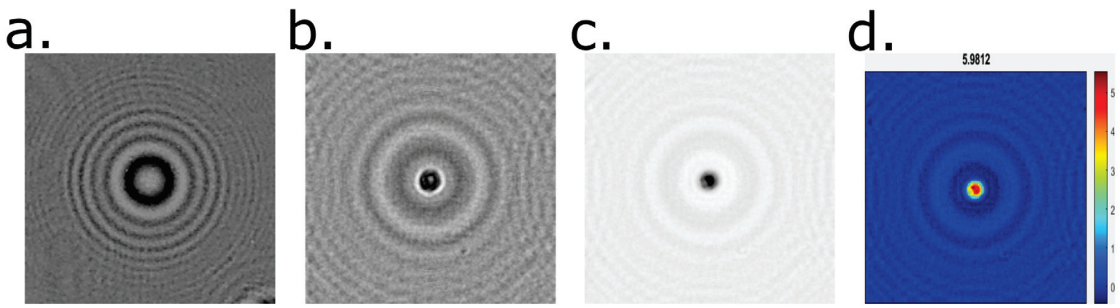

Figure 3.3: Reconstructed images. a. Hologram red channel. b. Amplitude. c. Phase. d. Phase shift

From the numerical reconstruction results, it is seen that the sub-cellular structure of cells is highly suppressed. Also, the cell boundaries are not very clear when the small distance between real and twin images is considered. This small distance between the object to the hologram plane will cost an extra loss due to the frequency components of the twin image term. The background of the amplitude image is specific to the objects' z2 position. For the phase images, most of the reconstructed cell images have similar background profiles. The obtained phase shift values depend on the position of the particle, particle size, type, and the direction of the incoming wavelength.

The phase unwrapping results are specific to objects structure. To understand the phase shift effect from a simple illustration, the unwrapped phase shift value starting from 0 to 9.6 radian with 0.8 radian increments is used with a blue dot line in the Figure 3.4.a. The red line represents its discontinuous version to represent wrapped phase information. In the Figure 3.4.b., the wrapped image from the MDA-MB-231 cells is given. Corresponding unwrapped version by the unwrapping method (Zhao et al. 2018) is given in the Figure 3.4.c.

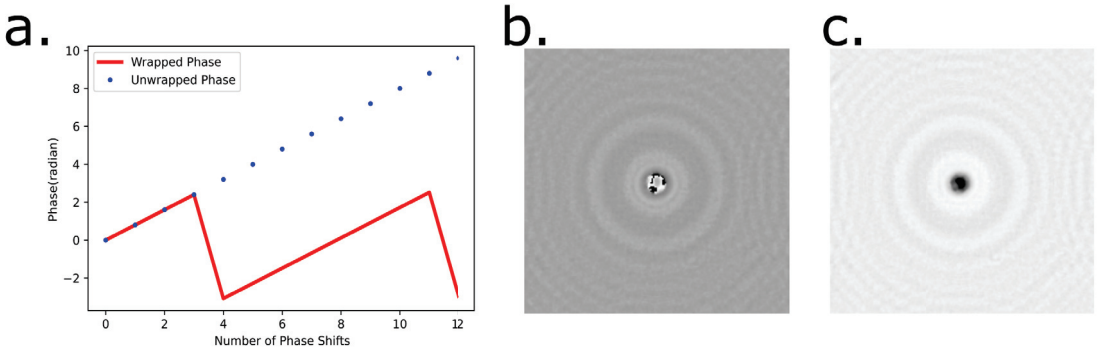

Figure 3.4: Phase unwrapping procedure. a. Phase unwrapping illustration of the phase shift increments (0.8 radian) - 12 times. b. Wrapped phase image. c. Unwrapped phase image

The success of the unwrapping method depends on the used function and its ability to determine the phase jumps. Another method from the work of Latychevskaia et al. is employed to check the validity of obtained results (Latychevskaia et al. 2010). In both phase unwrapping algorithms, very similar phase profiles are obtained. Therefore, for the rest of the thesis, the method of Zhao et al. is used.

3.1.3 Single and Multi-shot Phase Retrieval Results

During the iterative reconstruction process, accurate masking, and background normalization is crucially important. Also, the number of iterations and the convergence of final results need to be evaluated with visual confirmation. Especially, it is important for large objects due to suppressed sub-cellular components (Mudanyali et al. 2010). Different from the normal reconstruction process, sharpest point reconstruction is not giving the correct results in the iterative phase retrieval process. Therefore, crosschecking

with the brightfield counterparts would provide more accurate results. The result of the iterative retrieval from the MDA-MB-231-MB-231 cell hologram is given with the hologram, iteratively retrieved phase and brightfield counterparts given in the Figure 3.5.a,b,c respectively.

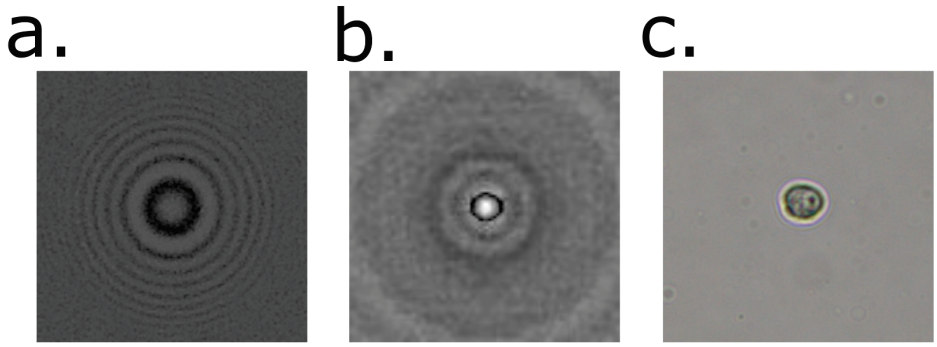

Figure 3.5: Single shot iterative phase retrieval. a. Hologram, b. Single-shot phase retrieval, c. Brightfield counterpart

In addition to applying background normalization as a source of constraint, it is possible to induce different constraints in these iterative measurements to fasten the convergence. For example, since most of the objects have positive absorption, it can be used as an additional constraint in the object plane while updating the iteration process (Latychevskaia 2019). The comparison of the directly reconstructed images with the iteratively phase retrieved counterparts is given in the Figure 3.6. A hologram image is given in the Figure 3.6.a with a direct reconstruction process for amplitude image is given in the Figure 3.6.b. Phase image is given in the Figure 3.6.c with the phase shift Figure 3.6.d in terms of radian. In the reconstructed images, two circular parts are clearly seen but the outer layers have noisy conditions. Object boundaries are not directly seen. Then, for the iterative retrieval process, a complement mask is given in the Figure 3.6.e with amplitude image given in the Figure 3.6.f, phase image given in the Figure 3.6.g, and phase shift given in the Figure 3.6.h in terms of radian. In the phase retrieved counterparts, object boundaries are clearly seen with the accurate shape information.

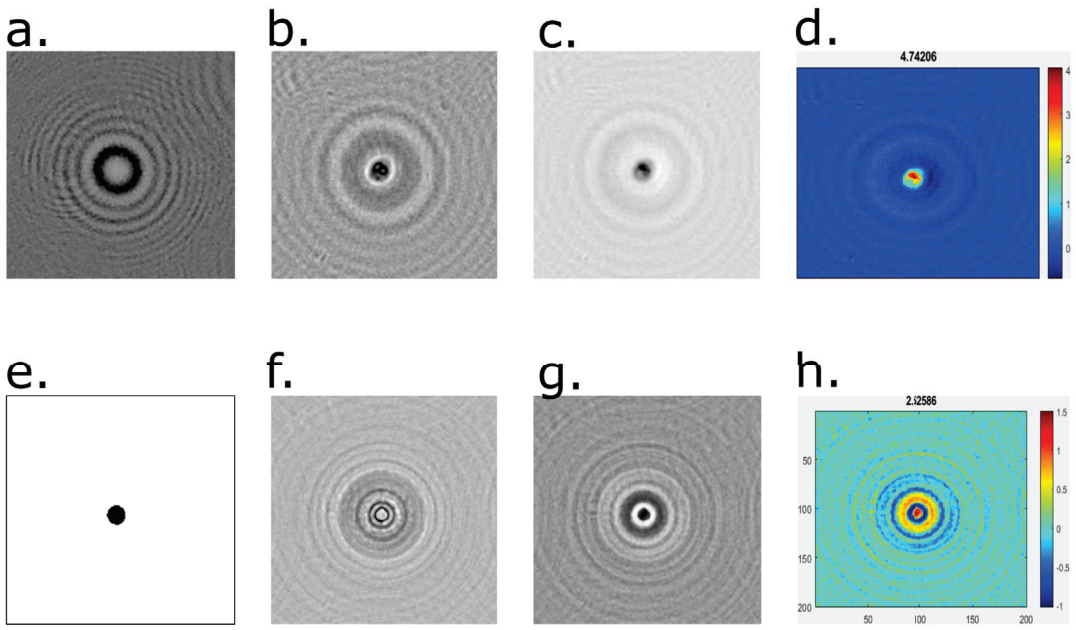

Figure 3.6: Comparison of the directly reconstructed images with iteratively retrieved counterparts. a. Hologram. b. Amplitude. c. Phase. d. Phase shift. e. Applied mask. f. Twin-image free amplitude. g. Twin image-free phase. h. Phase shift for twin-image free reconstruction

The respective multi-shot process is tried with partially coherent light sources that are aligned with multimode optical fiber to take 3 colors from the same output. A system with an RGB LED (Heliopto) with central wavelengths of 623nm and 455nm is used to obtain red, and blue holograms respectively. For spatial filtering of incoherent light, multimode optical fiber with a core diameter of 400 µm is used. (Ocean Optics, QP400-025-SR-BX) LED and optical fiber are aligned by using a 3D printed housing (Formlabs Form 2, USA). The tip of the optical fiber and the imaging sensor is 5 cm apart from each other to converge paraxial wave approximation to obtain plane waves at the sample plane. The same camera board is used during this experimental part. In the Figure 3.7.a, the reconstructed amplitude from blue LED is given. In the Figure 3.7.b., the reconstructed amplitude for red LED is given. In the last Figure 3.7.c, their combined process for the applied multiwavelength iterative retrieval is given.

Although the object structure is revealed during this iterative process, the noise is boosted to suppress the contrast of the resulting twin-image-free reconstructed image. Different from the works of Zhang et al., no wiener filtering is used in this method (Ghiglia and Romero 1994). Also, respective reconstructed images for blue and red channels have different phase shift responses as visually seen from the figures. Also, the usage of LED

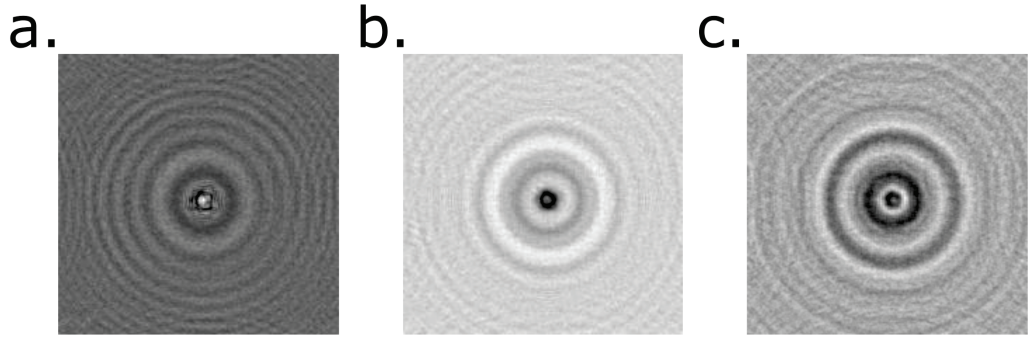

Figure 3.7: Multi-wavelength iterative retrieval results. a. Blue wavelength (460 nm) reconstruction. b. Red wavelength (630 nm) reconstruction. c. Multi-shot retrieval results

has limited the probability of controlling the illumination intensity. Therefore, these small differences have affected the final quality of the multi-wavelength phase retrieval process.

3.2 Conditional-GAN Based Phase Transformation

The computational workload of one-by-one iterative retrieval for each cell is hard to implement. As an alternative, the conditional GAN model is trained to obtain weights so that it can be used later to directly convert iteratively reconstructed images into phase retrieved ones. In this way, the direct transformation from reconstructed images to phase retrieved counterparts can be obtained easily. For this purpose, initially, the model for the Amplitude to Phase (model 1) is used to obtain mSSIM value of 0.673 for the quality control dataset (test). The obtained mean SSIM values per 50 epochs for the amplitude to conversion model are plotted in the Figure 3.8.a. The corresponding comparison of Target (reconstructed phase) vs Source (reconstructed amplitude) mSSIM is given in the Figure 3.8.b. Target vs Prediction (generated image) mSSIM is given in the Figure 3.8.c. Respective source, target, and generated phase images are given in the Figure 3.8.d,e,f.

In the second model, the obtained results for the model of reconstructed phase images are converted to phase retrieved images (model 2) that have mSSIM value of 0.324 for the quality control dataset (test). The obtained mean SSIM values per 200 epochs for the amplitude to conversion model are plotted in the Figure 3.9.a. The corresponding example of Target (phase retrieved image) vs Source (reconstructed phase image) mSSIM value is given in the Figure 3.9.b. Target vs Prediction (generated image) mSSIM value is given in the Figure 3.9.c. Respective source, target, and generated phase images are given in the Figure 3.9.d,e,f.

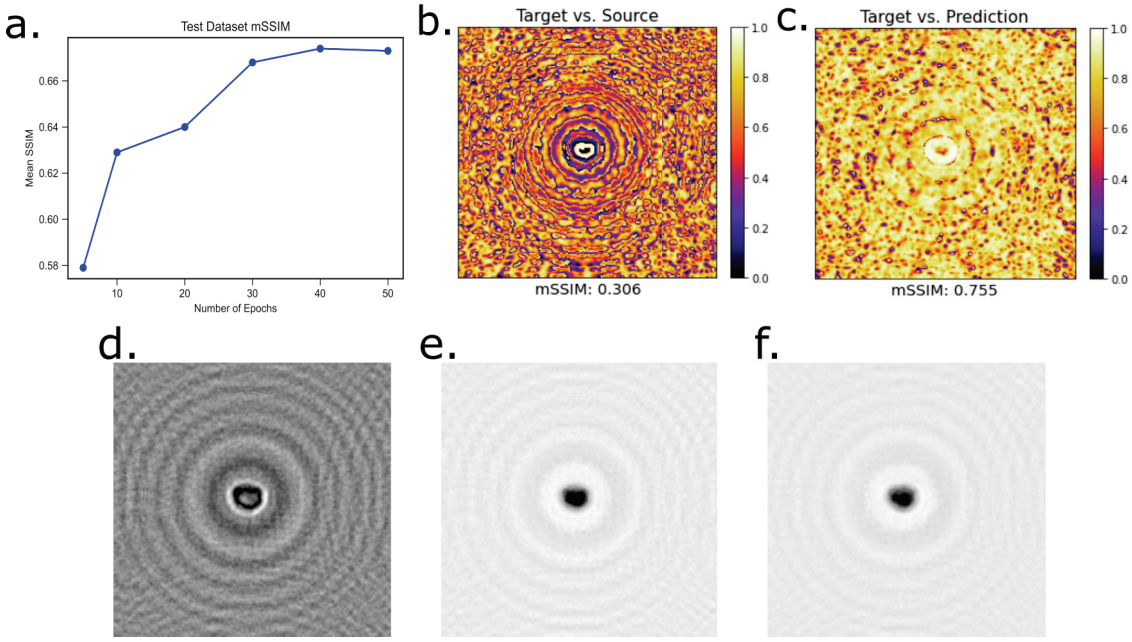

Figure 3.8: Amplitude to phase conversion model. a. Mean SSIM for 50 epochs. b. Target vs source mSSIM. c. Target vs prediction mSSIM. d. Amplitude. e. Target. f. Prediction

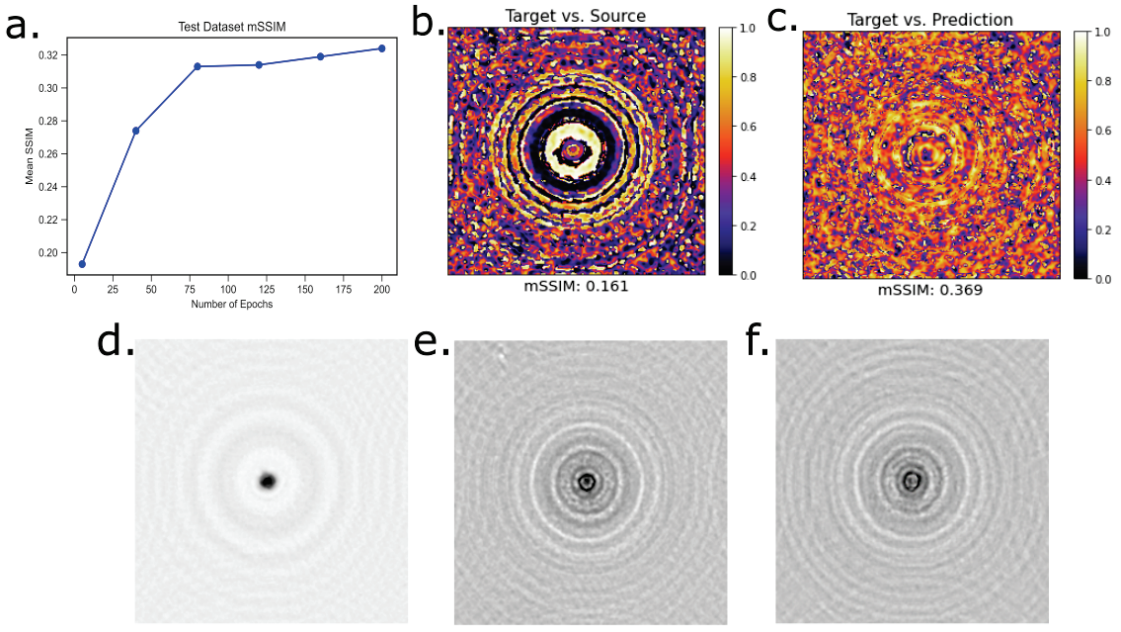

Figure 3.9: Reconstructed phase to phase retrieved conversion model. a. Mean SSIM for a50 epochs. b. Target vs source mSSIM. c. Target vs prediction mSSIM. d. Amplitude. e. Target. f. Prediction

In the used conditional image translation model, amplitude images to phase images or phase images to twin-image free counterparts are obtained. The second one is more important in LDIHM applications to lessen the burden of computing. But the obtained

results were not good enough and still require hyperparameter optimizations. Although different parameters have been tried, the maximum value obtained for the amplitude to phase images remained at 0.673 mSSIM and 0.324 for phase images to twin-image free counterparts. The reason for this kind of low score has different reasons that may be related to the dataset size. mSSIM value takes the 11 surrounding pixels from each point of the image, and it gives us collective similarity results. At this point, predicted images are not able to obtain the details of objects properly especially when the small object sizes are taken into consideration. The generated images are able to predict the background very well but give problematic predictions on the object's shape especially for the second model. Moreover, the used dataset of the reconstructed phase to phase retrieved images do not have uniform intensity profiles therefore it leads to a decrease in the final obtained mSSIM values. This non-uniformity especially dominates the phase retrieved twin image results to remain in the 0.324 bands. With more proper and increased dataset sizes, it is possible to obtain better mSSIM values. As an additional step, initially trained cGAN neural network weights can be used with cloud-based platforms to provide immediate results (Shimahara et al. 2019). These pre-trained weights could be uploaded to the website, amplitude images can be given to convert them into phase retrieved counterparts.

3.3 Classification and Detection Results

Accuracy and loss values for train and validation sets are given in the Figure 3.10.a. These values indicate the normalized correct predictions. Then, the trained structure is tested with untrained test data. In the confusion matrix Figure 3.10.b, actual and predicted correctly as MDA-MB-231 represent True Negative (TN). The one that is actual and correctly predicted as U937 is called True Positive (TP). If the cell is MDA-MB-231 and predicted as U937, it is called False Positive (FP). In the reverse condition, if the cell is U937 and predicted as MDA-MB-231 it is called False Negative (FN). These terms are taken together to understand how well the trained network classify.

In this analysis, precision is taken as to how well the neural model classified the correct predictions which is calculated from the Eq. 3.1.

$$Precision = \frac{TP}{TP + FP} \tag{3.1}$$

The recall is another factor and it calculates the ratio of how many actual U937 cells are labeled correctly which is calculated from the Eq. 3.2.

$$Recall = \frac{TP}{TP + FN} \tag{3.2}$$

F1 score calculates the balance between precision and recall values by taking a harmonic mean of these values with the Eq. 3.3.

$$F1 - Score = 2 * \frac{Precision * Recall}{Precision + Recall} \tag{3.3}$$

From the classification part; precision, recall, and F1-Score values are found to be 0.93 that is given in average in the Figure 3.10.c.

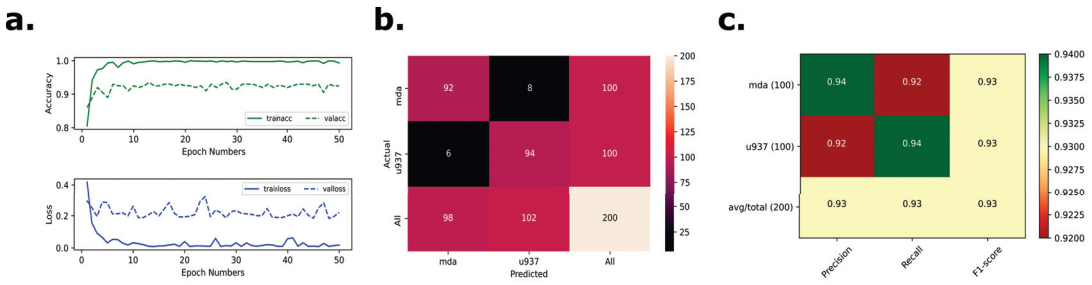

Figure 3.10: Classification results for test images. a. Accuracy and loss graphs for train and val values. b. Confusion matrix for test dataset. c. Precision, recall and f1 score for test dataset

In the classification step, obtained set of holograms are directly fed into the Resnet 34 model and 93% accuracy is obtained. But the initial dataset was quite heterogeneous and some of the cropped holograms were consists of dust particles or dead cells. Therefore, obtaining such good results proven the generalization capacity of classification models with error-prone structures. Especially, the small dust particles tend to be taken as U937 cells which creates problematic consequences. Therefore, the results are indicative and they all need to be quantified before making an appropriate consequence.

From the object detection part of the YOLO, train class loss and mAP .5 values are given in the Figure 3.11.a. Obtained precision, recall, mAP for 0.5, and mAP for 0.95

values are given to show the efficiency of the model which is given in the Figure 3.11.b. Also, the MDA-MB-231 cells with their confidence results are given in the Figure 3.11.c. In the Figure 3.11.d., confidence results for the U937 cells are given.

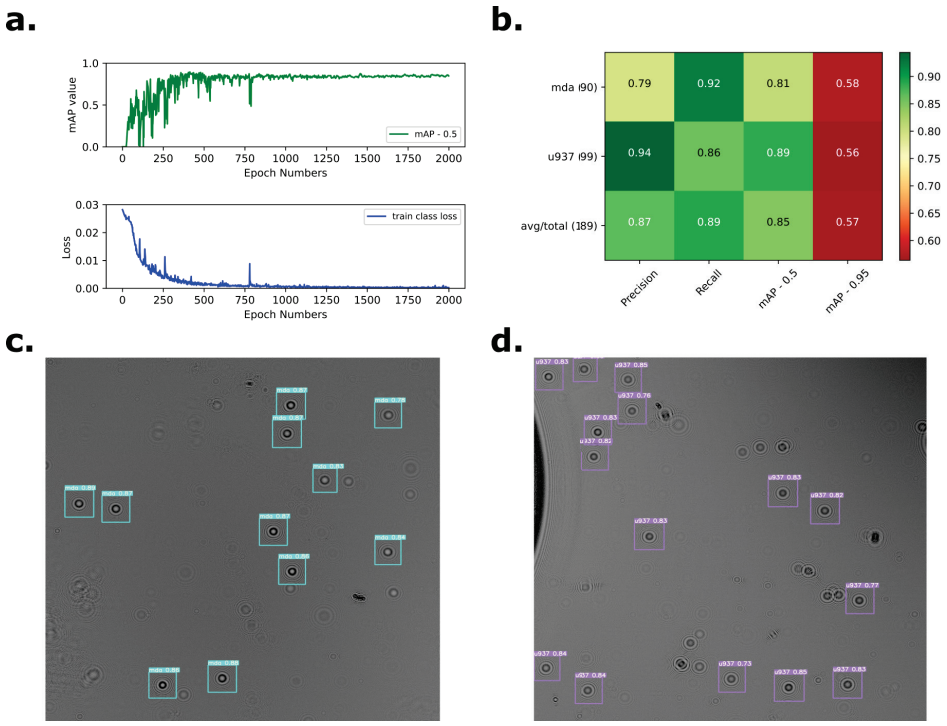

Figure 3.11: YOLO object detection results. a. mAP and loss graphs for training. b. Precision, recall, mAP for 0.5 and 0.95 results. c. MDA-MB-231 object detection. d. U937 object detection

From the object detection part results, total precision and recall values are found to be 0.87 and 0.89 respectively with an mAP of 0.85. Since some of the cells represent dust or problematic particles etc., the obtained results give us better-approximated results when it is compared to classification part results. The distance between two particles is generally taken as large enough to not affect each other in terms of the holographic diffraction pattern. Therefore, the obtained results are unable to detect all cells especially the intertwined ones. These intertwined cell holograms are not able to reconstruct or phase retrieved directly because their interferometric patterns are affected each other. The solution to this problem lies upon the multi-height process (Greenbaum et al. 2012) which has not been performed throughout the thesis studies yet. Therefore, I have tried to annotate similar objects with the classification dataset. Therefore, the result of YOLO object detection can be increased with more proper labeling steps.

3.4 Characteristics of Cells

From the phase shift-based elimination step, phase shift values below 2.06 radian for MDA-MB-231 and 1.48 radian for U937 cells are eliminated with the percentage error steps. Most of the eliminated ones are represent dust particles, as well as some of them, have a low-SNR ratio to limit the effective reconstruction. In total of 150 images for the MDA-MB-231 cells and 183 images for U937 cells images are eliminated.

In the second step, due to the low-SNR ratio of cells and indetectable object existence, some of the images are disregarded. Although binary masks are obtained for whole-cells, some of the masks do not represent any cell structure or they don't maintain the region props threshold value of Matlab function which is selected as 0.98. A total of 10 images for MDA-MB-231 and 33 for U937 images are eliminated within this step.

The mean value of perimeter for MDA-MB-231 images is found to be 48.15 and 42.87 for U937 cell images. With the 50 percent error elimination mechanism, perimeter values below 24.07 for MDA-MB-231 and 21.43 for U937 are eliminated because the corresponding cells can't be that much smaller. In total of 9 cells are eliminated from MDA-MB-231 cell images and 5 images eliminated for U937 cell images.

In the circularity-based elimination step, the mean circularity value for MDA-MB-231 cells is 0.964 and the mean circularity for U937 cells is 0.957. The one that cannot represent the cells is selected to be 0.482 for MDA-MB-231 and 0.478 for U937 from the circularity values of cells. Then, 50 percent error elimination is used and 2 MDA-MB-231 images and 9 U937 images are eliminated.

With the quantitative analysis model, problematic images are eliminated without the visual confirmation step. Therefore, the proposed model tends to become an automated model with integrated steps in future work. From the total of 954 images for each cell, 171 are eliminated from MDA-MB-231 cells and 226 are eliminated from U937 cells which is given in the Figure 3.12.a. The remaining 783 images for MDA-MB-231 and 728 images for U937 are analyzed to understand final phase shift, perimeter, and circularity values. For MDA-MB-231 cells, the mean value of phase shift is found to be 4.67 radians with a standard error of 1.38 radians and 3.44 mean for U937 cells with a standard error of 1.36 radian is given in the Figure 3.12.b. Corresponding mean perimeter values are 48.44 for MDA-MB-231 with a standard error of 6.91 and 42.85 mean for U937 with a standard error of 8.98 is given in the Figure 3.12.c. The obtained mean circularity value is 0.9645 for MDA-MB-231 cells with a standard deviation of 0.097 and 0.9604 mean for U937 cells with a standard deviation of 0.1008 is given in the Figure 3.12.d.

In the performed analysis, the initial and the most important differentiation mechanism is based on using the phase shift values. In the literature, evaluation of MDA-MB-231 and U937 cells are not directly performed from phase shift values before. But from the

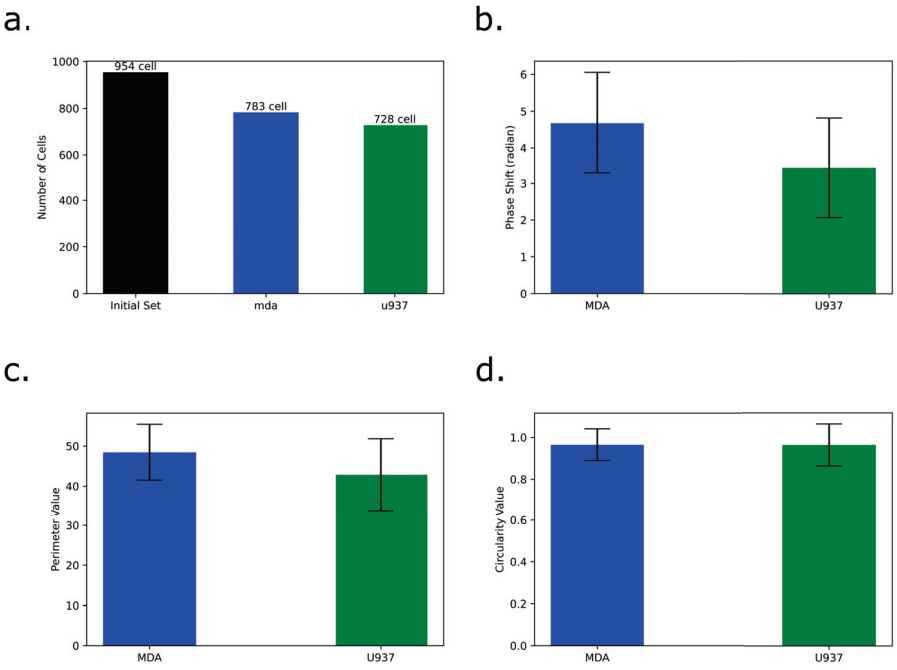

Figure 3.12: Morphological values of cells. a. Final dataset sizes. c. Mean perimeter values. d. Mean circularity values

experimental findings, it is known that inline holography with laser usage can underestimate the acquired phase shift around 20% (Zhang et al. 2018). So, it can be expected to more for the partially-coherent LED source. However, since the perimeter value is directly related to the diameter value of cells, it can be used as an indicative value. From the previous studies of MDA-MB-231 cells, the mean diameter is found to be 17 μm (Ozbey et al. 2019). For the U937 cells, this average value is found to be 14 μm (Lee et al. 2018). Thus, the corresponding comparison can be approximated with the circular shape assumption of cells and the similarity between thickness and diameter. Corresponding thickness equation is calculated using the Eq. 3.4:

$$t = \frac{\Delta\phi * \lambda}{2 * \pi * |(n_o - n_m)|} \tag{3.4}$$

where the phase shift ($\Delta\phi$) found from cells are used with refractive index difference between medium (n_m) and object (n_o) to find thickness values. λ is the wavelength of the light source.

The mean phase shift value for the MDA-MB-231 cells is found to be 4.67 radians. The refractive index of the MDA-MB-231-MB-231 cells is found to be 1.38 from the literature (Zouggari Ben El Khyat 2019). DI water refractive index at 590 nm is 1.33. Therefore, the corresponding thickness value for MDA-MB-231 is found to be 2.48

μm. The refractive index of the U937 cells is found to be 1.38 from the literature (Kuś et al. 2014). Therefore, the corresponding thickness value is found to be 1.83 μm. The obtained thickness values are relatively low because the complete phase retrieval measurement step from different points has not been performed. Also, the usage of a partially coherent light source limits the obtained phase shift value. With laser usage, these phase shift values can be better approximated.

For the perimeter and circularity measurements, corresponding diameter values for MDA-MB-231 and U937 cells were found from the literature to make an indicative comparison based on a normalized ratio. Mean perimeter value ratios between MDA-MB-231 and U937 cells are found to be 1.13 in our final dataset. In the literature, the mean diameter ratio between these cells is around 1.21. So, the error rate of 7% is achieved which is quite good for such a simple system when we consider the existence of twin image artifacts and circularity values of cells.

3.5 Quantitative Classification Results

Throughout the thesis, the initial classification model can obtain 93 % accuracy on test data. But the actual value can be lower than the obtained value. Because the initial data contain mostly dust particles, high SNR ratio images, dead cells, and irregular shaped objects. Therefore, the proposed system is used to eliminate these problematic cells from the initial dataset. Then, the final dataset obtained from the quantitative analysis part is used in Resnet 34 model with the same parameters performed in the initial dataset. Train:Val:Test splits set to become 576:72:72 to maintain initial ratios. A batch size of 32 is used. The initial learning rate set to be 0.001, momentum is taken as 0.9, and as an optimizer SGD model is used. During training, TESLA P100-PCI-E is used and it takes 210 seconds to process 50 epochs. The obtained results are given below. in Figure, accuracy and loss values for train and validation datasets are given which give us final validation accuracy of 0.921 that is given in the Figure 3.13.a for accuracy and loss values. Then, the trained structure is tested with blind test data. The obtained confusion matrix is given in the Figure 3.13.b. Respective f1-score, precision, and recall values are found to be 0.92 on average as shown in the Figure 3.13.c.

Around 25% of the initial dataset is eliminated during the analysis part but almost the same precision is achieved with the same classification model. When the initial dataset is compared with the final dataset, 20 test images are eliminated from MDA-MB-231 cells, and 24 of the images are eliminated from the U937 cells. The initial test data is kept fixed so that it can be compared to the final quantitative results. Since 20 test images were

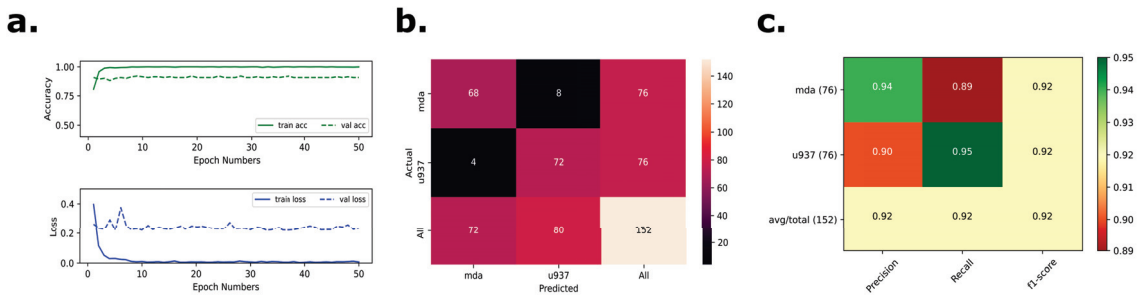

Figure 3.13: Morphological values of cells. a. Final dataset sizes. c. Mean perimeter values. d. Mean circularity values

eliminated, the expected precision value needs to be around 80% in the initial set. But the obtained initial and final precision values are around 92% to 93%. Therefore, one needs to be careful while using such deep learning models directly in clinical studies when the huge error rate between the quantitative and classified results is considered. Also, in order to give more interpretable results, interference studies of neural network model could be used to reveal how the neural model learn to differentiate these cells.

CHAPTER 4

CONCLUSION

The LDIHM has been a promising computational imaging tool with easy-to-fabricate, cost-effective, and portable design. The total cost of building such a simple setup is around 350 $ (See3CAM-CU135 camera board - 250 $, Pinhole 62.75 $ and LED 17.27 $). Therefore, the optical setup could be used as a POC device in resource-limited areas for the analysis of micron-sized objects. Therefore, as an initial step, the optimization of the LDIHM setup has been performed.

From the acquired holograms of MDA-MB-231 and U937 cells; the numerical reconstruction, phase unwrapping, and phase retrieval processes have been performed. Direct cell holograms are trained with the Resnet34 classification model to achieve 0.93 precision on blind test data. Also, with the same dataset on the YOLO object detection algorithm, mAP of 0.87 is achieved at 0.5 thresholds for the whole cells. In addition, the pix2pix conditional GAN model was used to obtain the mSSIM value of 0.673 for the reconstructed amplitude to phase conversion model. With the same conversion model, the reconstructed phase to phase retrieved model is obtained mSSIM value of 0.324. From the quantitative analysis part, a mean phase shift radian of 4.67, perimeter value of 48.15, and circularity value of 0.964 are measured for MDA-MB-231 cells. For U937 cells, 3.44 radian phase shift, 42.97 perimeter, and 0.960 circularity values are measured.

The further interest will be based upon creating the same dataset with brightfield counterparts to obtain more accurate results in the iterative phase retrieval step. Instead of directly reconstructed phase images, phase retrieved images can be analyzed with more accurate perimeter and circularity values. With a large amount of data, the success of c-GAN models can be increased. Most importantly, all of these processes can be integrated into semi-supervised learning models with further studies. The initial neural network model can be used to detect, reconstruct and eliminate twin image artifacts of cells. The proposed second model can be used to differentiate objects from quantitative information. Therefore, such a proposed analysis model will lessen the burden of computing and provide quantitative results efficiently.

In summary, LDIHM is used to differentiate the MDA-MB-231 and U937 cells quantitatively. The proposed model can be used for the detection of cancer cells in the presence of blood cells that can be further applied for CTC detection. Also, the quantification model can be applied for different cell types for different disease diagnoses.

REFERENCES

Lockyer, Sir Norman. 1976. *Nature Volume 14*. Nature.

Vangindertael, J, R Camacho, W Sempels, H Mizuno, P Dedecker, and K P F Janssen. 2018. "An introduction to optical super-resolution microscopy for the adventurous biologist." *Methods and Applications in Fluorescence* 6 (2): 022003.

"The quest for quantitative microscopy." 2012. *Nature Methods* 9:627–627.

Hu, Xue-mei, Jia-min Wu, Jin-li Suo, and Qiong-hai Dai. 2017. "Emerging theories and technologies on computational imaging." *Frontiers of Information Technology & Electronic Engineering* 18, no. 9 (September): 1207–1221.

Coskun, Ahmet F, and Aydogan Ozcan. 2014. "Computational imaging, sensing and diagnostics for global health applications." Analytical biotechnology, *Current Opinion in Biotechnology* 25:8–16.

Young, Thomas. 1802. "II. The Bakerian Lecture. On the theory of light and colours." *Philosophical Transactions of the Royal Society of London* 92 (December): 12–48.

Michelson, Albert A., and Edward W. Morley. 1887. "LVIII. On the relative motion of the earth and the luminiferous Eather." *The London, Edinburgh, and Dublin Philosophical Magazine and Journal of Science* 24, no. 151 (December): 449–463.

GABOR, D. 1948. "A New Microscopic Principle." *Nature* 161, no. 4098 (May): 777–778.

Kim, Myung K. 2010. "Principles and techniques of digital holographic microscopy." *SPIE Reviews* 1 (January): 018005.

Leith, Emmett N., and Juris Upatnieks. 1963. "Wavefront Reconstruction with Continuous-Tone Objects∗." *J. Opt. Soc. Am.* 53, no. 12 (December): 1377–1381.

Anand, A., V. K. Chhaniwal, N. R. Patel, and B. Javidi. 2012. "Automatic Identification of Malaria-Infected RBC With Digital Holographic Microscopy Using Correlation Algorithms." *IEEE Photonics Journal* 4, no. 5 (October): 1456–1464.

El-Schich, Zahra, Anna Leida Mölder, and Anette Gjörloff Wingren. 2018. "Quantitative Phase Imaging for Label-Free Analysis of Cancer Cells—Focus on Digital Holographic Microscopy." *Applied Sciences* 8 (7).

Schnars, U., and W. Jüptner. 1994. "Direct recording of holograms by a CCD target and numerical reconstruction." *Applied Optics* 33, no. 2 (January): 179.

Zhang, Tong, and Ichirou Yamaguchi. 1998. “Three-dimensional microscopy with phase-shifting digital holography.” *Opt. Lett.* 23, no. 15 (August): 1221–1223.

Xu, Wenbo, M. H. Jericho, I. A. Meinertzhagen, and H. J. Kreuzer. 2001. “Digital in-line holography for biological applications.” *Proceedings of the National Academy of Sciences* 98 (20): 11301–11305.

Peruhov, Iliyan, and Emilia Mihaylov. 2013. “Applications of Holographic Microscopy in Life Sciences.” In *Holography - Basic Principles and Contemporary Applications.* InTech, May.

Garcia-Sucerquia, Jorge, Wenbo Xu, Stephan K. Jericho, Peter Klages, Manfred H. Jericho, and H. Jürgen Kreuzer. 2006. “Digital in-line holographic microscopy.” *Appl. Opt.* 45 (5): 836–850.

Garcia-Sucerquia, J., W. Xu, S. K. Jericho, M. H. Jericho, and He J. Kreuzer. 2008. “4-D imaging of fluid flow with digital in-line holographic microscopy.” *Optik* 119, no. 9 (July): 419–423.

Seo, Sungkyu, Ting-Wei Su, Derek K. Tseng, Anthony Erlinger, and Aydogan Ozcan. 2009. “Lensfree holographic imaging for on-chip cytometry and diagnostics” [in eng]. 19255659[pmid], *Lab on a chip* 9 (6): 777–787.

Lai, Songcan, Björn Kemper, and Gert von Bally. 2000. “Twin-image Elimination in Digital In-line Holography.” In *Optics and Lasers in Biomedicine and Culture,* 79–82. Springer Berlin Heidelberg.

Hennelly, B., D. Kelly, N. Pandey, and D. S. Monaghan. 2009. “Review of Twin Reduction and Twin Removal Techniques in Holography.”

Gerchberg, R. 1972. “A practical algorithm for the determination of phase from image and diffraction plane pictures.” *Optik* 35:237–246.

Liu, G., and P. Scott. 1987. “Phase retrieval and twin-image elimination for in-line Fresnel holograms.” *Journal of The Optical Society of America A-optics Image Science and Vision* 4:159–165.

Teague, M. R. 1983. “Deterministic phase retrieval: a Green’s function solution.” *Journal of the Optical Society of America (1917-1983)* 73 (November): 1434.

Fienup, J. 1982. “Phase retrieval algorithms: a comparison.” *Applied optics* 21 15:2758–69.

Greenbaum, Alon, Wei Luo, Ting-Wei Su, Zoltán Göröcs, Liang Xue, Serhan O Isikman, Ahmet F Coskun, Onur Mudanyali, and Aydogan Ozcan. 2012. "Imaging without lenses: achievements and remaining challenges of wide-field on-chip microscopy." *Nature Methods* 9, no. 9 (August): 889–895.

Latychevskaia, Tatiana, and Hans-Werner Fink. 2007. "Solution to the Twin Image Problem in Holography." *Physical Review Letters* 98, no. 23 (June).

Latychevskaia, Tatiana, and Hans-W Fink. 2015. "Practical algorithms for simulation and reconstruction of digital in-line holograms." *Appl. Opt.* 54 (9): 2424–2434.

Mudanyali, Onur, Derek Tseng, Chulwoo Oh, Serhan O. Isikman, Ikbal Sencan, Waheb Bishara, Cetin Oztoprak, Sungkyu Seo, Bahar Khademhosseini, and Aydogan Ozcan. 2010. "Compact, light-weight and cost-effective microscope based on lensless incoherent holography for telemedicine applications." *Lab on a Chip* 10 (11): 1417.

Li, Weichang, Nick C. Loomis, Qiao Hu, and Cabell S. Davis. 2007. "Focus detection from digital in-line holograms based on spectral l1 norms." *J. Opt. Soc. Am. A* 24 (10): 3054–3062.

Dubois, Frank, Cédric Schockaert, Natacha Callens, and Catherine Yourassowsky. 2006. "Focus plane detection criteria in digital holography microscopy by amplitude analysis." *Opt. Express* 14 (13): 5895–5908.

Kan, Andrey. 2017. "Machine learning applications in cell image analysis." *Immunology & Cell Biology* 95, no. 6 (April): 525–530.

Kraus, Oren Z., Jimmy Lei Ba, and Brendan J. Frey. 2016. "Classifying and segmenting microscopy images with deep multiple instance learning." *Bioinformatics* 32, no. 12 (June): i52–i59.

Meijering, Erik. 2020. "A bird's-eye view of deep learning in bioimage analysis." *Computational and Structural Biotechnology Journal* 18:2312–2325.

Rosenblatt, F. 1957. *The perceptron - A perceiving and recognizing automaton.* Technical report 85-460-1. Ithaca, New York: Cornell Aeronautical Laboratory.

Minsky, Marvin, and Seymour Papert. 1987. "Perceptrons: an introduction to computational geometry, expanded edition." *Editorial The MIT Pres. Libro publicado* 28.

Werbos, P.J. 1975. *Beyond Regression: New Tools for Prediction and Analysis in the Behavioral Sciences.* Harvard University.

LeCun, Y., B. Boser, J. S. Denker, D. Henderson, R. E. Howard, W. Hubbard, and L. D. Jackel. 1989. "Backpropagation Applied to Handwritten Zip Code Recognition." *Neural Computation* 1 (4): 541–551.

Hochreiter, Sepp. 1998. "The vanishing gradient problem during learning recurrent neural nets and problem solutions." *International Journal of Uncertainty, Fuzziness and Knowledge-Based Systems* 6 (02): 107–116.

Hinton, Geoffrey E., Simon Osindero, and Yee-Whye Teh. 2006. "A Fast Learning Algorithm for Deep Belief Nets." *Neural Computation* 18, no. 7 (July): 1527–1554.

Deng, Jia, Wei Dong, Richard Socher, Li-Jia Li, Kai Li, and Li Fei-Fei. 2009. "ImageNet: A large-scale hierarchical image database." In *2009 IEEE Conference on Computer Vision and Pattern Recognition.* IEEE, June.

LeCun, Yann, Yoshua Bengio, and Geoffrey Hinton. 2015. "Deep learning." *Nature* 521, no. 7553 (May): 436–444.

Sinha, Ayan, Justin Lee, Shuai Li, and George Barbastathis. 2017. "Lensless computational imaging through deep learning." *Optica* 4 (9): 1117–1125.

Rivenson, Yair, Yibo Zhang, Harun Günaydın, Da Teng, and Aydogan Ozcan. 2017. "Phase recovery and holographic image reconstruction using deep learning in neural networks." *Light: Science & Applications* 7, no. 2 (October): 17141–17141.

Wu, Yichen, and Aydogan Ozcan. 2018. "Lensless digital holographic microscopy and its applications in biomedicine and environmental monitoring." *Methods* 136 (March): 4–16.

Gorocs, Zoltan, Miu Tamamitsu, Vittorio Bianco, Patrick Wolf, Shounak Roy, Koyoshi Shindo, Kyrollos Yanny, et al. 2018. "A deep learning-enabled portable imaging flow cytometer for cost-effective, high-throughput, and label-free analysis of natural water samples." *Light: Science & Applications* 7 (1).

Rivenson, Yair, Tairan Liu, Zhensong Wei, Yibo Zhang, Kevin de Haan, and Aydogan Ozcan. 2019. "PhaseStain: the digital staining of label-free quantitative phase microscopy images using deep learning." *Light: Science & Applications* 8, no. 1 (February).

Huang, Luzhe, Tairan Liu, Xilin Yang, Yi Luo, Yair Rivenson, and Aydogan Ozcan. 2021. "Holographic Image Reconstruction with Phase Recovery and Autofocusing Using Recurrent Neural Networks." *ACS Photonics* 8, no. 6 (May): 1763–1774.

Lam, Van K., Thanh C. Nguyen, Vy Bui, Byung Min Chung, Lin-Ching Chang, George Nehmetallah, and Christopher B. Raub. 2020. "Quantitative scoring of epithelial and mesenchymal qualities of cancer cells using machine learning and quantitative phase imaging." *Journal of Biomedical Optics* 25 (02): 1.

Viola, P., and M. Jones. 2001. "Rapid object detection using a boosted cascade of simple features." In *Proceedings of the 2001 IEEE Computer Society Conference on Computer Vision and Pattern Recognition. CVPR 2001.* IEEE Comput. Soc.

Szegedy, Christian, A. Toshev, and D. Erhan. 2013. "Deep Neural Networks for Object Detection." In *NIPS.*

Girshick, Ross, Jeff Donahue, Trevor Darrell, and Jitendra Malik. 2014. "Rich Feature Hierarchies for Accurate Object Detection and Semantic Segmentation." In *2014 IEEE Conference on Computer Vision and Pattern Recognition.* IEEE, June.

Ren, Shaoqing, Kaiming He, Ross Girshick, and Jian Sun. 2017. "Faster R-CNN: Towards Real-Time Object Detection with Region Proposal Networks." *IEEE Transactions on Pattern Analysis and Machine Intelligence* 39, no. 6 (June): 1137–1149.

Redmon, Joseph, Santosh Divvala, Ross Girshick, and Ali Farhadi. 2016. "You Only Look Once: Unified, Real-Time Object Detection." In *Proceedings of the IEEE Conference on Computer Vision and Pattern Recognition (CVPR).*

Goodfellow, I., Jean Pouget-Abadie, Mehdi Mirza, Bing Xu, David Warde-Farley, S. Ozair, Aaron C. Courville, and Yoshua Bengio. 2014. "Generative Adversarial Nets." In *NIPS.*

Radford, Alec, Luke Metz, and Soumith Chintala. 2016. "Unsupervised Representation Learning with Deep Convolutional Generative Adversarial Networks." *CoRR* abs/1511.06434.

Hughes, Rowan T., Liming Zhu, and Tomasz Bednarz. 2021. "Generative Adversarial Networks–Enabled Human–Artificial Intelligence Collaborative Applications for Creative and Design Industries: A Systematic Review of Current Approaches and Trends." *Frontiers in Artificial Intelligence* 4 (April).

Wu, Yichen, Yilin Luo, Gunvant Chaudhari, Yair Rivenson, Ayfer Calis, Kevin de Haan, and Aydogan Ozcan. 2019. "Bright-field holography: cross-modality deep learning enables snapshot 3D imaging with bright-field contrast using a single hologram." *Light: Science & Applications* 8, no. 1 (March).

Sung, Hyuna, Jacques Ferlay, Rebecca L. Siegel, Mathieu Laversanne, Isabelle Soerjomataram, Ahmedin Jemal, and Freddie Bray. 2021. "Global Cancer Statistics 2020: GLOBOCAN Estimates of Incidence and Mortality Worldwide for 36 Cancers in 185 Countries." *CA: A Cancer Journal for Clinicians* 71, no. 3 (February): 209–249.

Zhong, Xiaoming, Hangtian Zhang, Ying Zhu, Yuqing Liang, Zhuolin Yuan, Jiachen Li, Jing Li, et al. 2020. "Circulating tumor cells in cancer patients: developments and clinical applications for immunotherapy." *Molecular Cancer* 19, no. 1 (January).

Fares, Jawad, Mohamad Y. Fares, Hussein H. Khachfe, Hamza A. Salhab, and Youssef Fares. 2020. "Molecular principles of metastasis: a hallmark of cancer revisited." *Signal Transduction and Targeted Therapy* 5, no. 1 (March).

Rodrigues, Paulo, and Sakari Vanharanta. 2019. "Circulating Tumor Cells: Come Together, Right Now, Over Metastasis." *Cancer Discovery* 9, no. 1 (January): 22–24.

Raub, Christopher B., and George Nehmetallah. 2017. "Holography, machine learning, and cancer cells." *Cytometry Part A* 91, no. 8 (April): 754–756.

Lopresti, Alexia, Fabrice Malergue, François Bertucci, Maria Lucia Liberatoscioli, Severine Garnier, Quentin DaCosta, Pascal Finetti, et al. 2019. "Sensitive and easy screening for circulating tumor cells by flow cytometry." *JCI Insight* 4, no. 14 (July).

Singh, Dhananjay Kumar, Caroline C. Ahrens, Wei Li, and Siva A. Vanapalli. 2017. "Label-free, high-throughput holographic screening and enumeration of tumor cells in blood." *Lab on a Chip* 17 (17): 2920–2932.

Cruz, Joseph A., and David S. Wishart. 2006. "Applications of Machine Learning in Cancer Prediction and Prognosis." *Cancer Informatics* 2 (January): 117693510600200.

Delikoyun, Kerem, Ersin Cine, Muge Anil-Inevi, Oyku Sarigil, Engin Ozcivici, and H. Cumhur Tekin. 2021a. "2 Deep learning-based cellular image analysis for intelligent medical diagnosis." In *Artificial Intelligence for Data-Driven Medical Diagnosis,* 19–54. De Gruyter.

Kourou, Konstantina, Themis P. Exarchos, Konstantinos P. Exarchos, Michalis V. Karamouzis, and Dimitrios I. Fotiadis. 2015. "Machine learning applications in cancer prognosis and prediction." *Computational and Structural Biotechnology Journal* 13:8–17.

Tripathy, Rajesh Kumar, Sailendra Mahanta, and Subhankar Paul. 2014. "Artificial intelligence-based classification of breast cancer using cellular images." *RSC Advances* 4 (18): 9349.

Rubin, Moran, Omer Stein, Nir A. Turko, Yoav Nygate, Darina Roitshtain, Lidor Karako, Itay Barnea, Raja Giryes, and Natan T. Shaked. 2019. "TOP-GAN: Stain-free cancer cell classification using deep learning with a small training set." *Medical Image Analysis* 57 (October): 176–185.

Ryle, J., Karen M. Molony, Susan L. McDonnell, T. Naughton, and John T. Sheridan. 2009. "Multispectral lensless digital holographic microscope: imaging MCF-7 and MDA-MB-231 cancer cell cultures." In *Optical Engineering + Applications.*

Schneider, B., G. Vanmeerbeeck, R. Stahl, L. Lagae, J. Dambre, and P. Bienstman. 2015. "Neural network for blood cell classification in a holographic microscopy system." In *2015 17th International Conference on Transparent Optical Networks (ICTON).* IEEE, July.

Song, Tzu Hsi, Mengzhi Cao, Jouha Min, Hyungsoon Im, Hakho Lee, and Kwonmoo Lee. 2021. "Deep Learning-Based Phenotyping of Breast Cancer Cells Using Lens-free Digital In-line Holography" (May).

Zhang, Hanqing, Tim Stangner, Krister Wiklund, and Magnus Andersson. 2018. "Object plane detection and phase retrieval from single-shot holograms using multi-wavelength in-line holography." *Applied Optics* 57, no. 33 (November): 9855.

Repetto, L., E. Piano, and C. Pontiggia. 2004. "Lensless digital holographic microscope with light-emitting diode illumination." *Optics Letters* 29, no. 10 (May): 1132.

Gorocs, Z., and A. Ozcan. 2013. "On-Chip Biomedical Imaging." *IEEE Reviews in Biomedical Engineering* 6:29–46.

Wu, Yichen, Yair Rivenson, Yibo Zhang, Zhensong Wei, Harun Günaydin, Xing Lin, and Aydogan Ozcan. 2018. "Extended depth-of-field in holographic imaging using deep-learning-based autofocusing and phase recovery." *Optica* 5, no. 6 (May): 704.

Popescu, Gabriel. 2019. "Gabor's holography at sea." *Light: Science & Applications* 8, no. 1 (January).

Goodman, Joseph W. 1968. *Introduction to Fourier optics.* McGraw-Hill.

Delikoyun, Kerem, Ali Aslan Demir, Engin Ozcivici, and Huseyin C Tekin. 2021b. "Lensless holographic microscopy." In *Imaging Modalities for Biological and Preclinical Research: A Compendium, Volume 1: Part I: Ex vivo biological imaging.* IOP Publishing.

Zhao, Zixin, Hangying Zhang, Zhaoxian Xiao, Hubing Du, Yiying Zhuang, Chen Fan, and Hong Zhao. 2018. “Robust 2D phase unwrapping algorithm based on the transport of intensity equation.” *Measurement Science and Technology* 30 (1): 015201.

Mirza, Mehdi, and Simon Osindero. 2014. “Conditional generative adversarial nets.” *arXiv preprint arXiv:1411.1784.*

Nazeri, Kamyar, Eric Ng, and Mehran Ebrahimi. 2018. “Image Colorization Using Generative Adversarial Networks.” In *Articulated Motion and Deformable Objects,* 85–94. Springer International Publishing.

Isola, Phillip, Jun-Yan Zhu, Tinghui Zhou, and Alexei A. Efros. 2017. “Image-to-Image Translation with Conditional Adversarial Networks.” In *2017 IEEE Conference on Computer Vision and Pattern Recognition (CVPR).* IEEE, July.

Chamier, Lucas von, Romain F. Laine, Johanna Jukkala, Christoph Spahn, Daniel Krentzel, Elias Nehme, Martina Lerche, et al. 2021. “Democratising deep learning for microscopy with ZeroCostDL4Mic.” *Nature Communications* 12, no. 1 (April).

Alzubaidi, Laith, Jinglan Zhang, Amjad J. Humaidi, Ayad Al-Dujaili, Ye Duan, Omran Al-Shamma, J. Santamaría, Mohammed A. Fadhel, Muthana Al-Amidie, and Laith Farhan. 2021. “Review of deep learning: concepts, CNN architectures, challenges, applications, future directions.” *Journal of Big Data* 8, no. 1 (March).

He, Kaiming, Xiangyu Zhang, Shaoqing Ren, and Jian Sun. 2016. “Deep Residual Learning for Image Recognition.” In *2016 IEEE Conference on Computer Vision and Pattern Recognition (CVPR).* IEEE, June.

Kaiming He, Shaoqing Ren, Xiangyu Zhang, and Jian Sun. 2016. “Identity Mappings in Deep Residual Networks.” In *Computer Vision – ECCV 2016,* 630–645. Springer International Publishing.

Jocher, Glenn, Alex Stoken, Jirka Borovec, NanoCode012, ChristopherSTAN, Liu Changyu, Laughing, et al. 2021. *ultralytics/yolov5: v4.0 - PyTorch Hub integration.*

Berg, Stuart, Dominik Kutra, Thorben Kroeger, Christoph N. Straehle, Bernhard X. Kausler, Carsten Haubold, Martin Schiegg, et al. 2019. “ilastik: interactive machine learning for (bio)image analysis.” *Nature Methods* 16, no. 12 (September): 1226–1232.

Bottema, M.J. 2020. “Circularity of objects in images.” In *2000 IEEE International Conference on Acoustics, Speech, and Signal Processing. Proceedings (Cat. No.00CH37100).* IEEE.

Latychevskaia, Tatiana, Petr Formanek, C.T. Koch, and Axel Lubk. 2010. “Off-axis and inline electron holography: Experimental comparison.” *Ultramicroscopy* 110, no. 5 (April): 472–482.

Latychevskaia, Tatiana. 2019. “Iterative phase retrieval for digital holography: tutorial.” *Journal of the Optical Society of America A* 36, no. 12 (November): D31.

Ghiglia, Dennis C., and Louis A. Romero. 1994. “Robust two-dimensional weighted and unweighted phase unwrapping that uses fast transforms and iterative methods.” *Journal of the Optical Society of America A* 11, no. 1 (January): 107.

Shimahara, Yuki, Ko Sugawara, Kei H. Kojo, Hiroki Kawai, Yuya Yoshida, Seiichiro Hasezawa, and Natsumaro Kutsuna. 2019. “IMACEL: A cloud-based bioimage analysis platform for morphological analysis and image classification.” Edited by Kaiming Li. *PLOS ONE* 14, no. 2 (February): e0212619.

Ozbey, Arzu, Mehrdad Karimzadehkhouei, Nur M. Kocaturk, Secil Erbil Bilir, Ozlem Kutlu, Devrim Gozuacik, and Ali Kosar. 2019. “Inertial focusing of cancer cell lines in curvilinear microchannels.” *Micro and Nano Engineering* 2 (March): 53–63.

Lee, Do-Hyun, Xuan Li, Alan Jiang, and Abraham P. Lee. 2018. “An integrated microfluidic platform for size-selective single-cell trapping of monocytes from blood.” *Biomicrofluidics* 12, no. 5 (September): 054104.

Zouggari Ben El Khyat, Chaymaa. 2019. “Stiffness study of cancer cells by osmotic shocks.” B.S. thesis.

Kuś, Arkadiusz, Michał Dudek, Björn Kemper, Małgorzata Kujawińska, and Angelika Vollmer. 2014. “Tomographic phase microscopy of living three-dimensional cell cultures.” *Journal of Biomedical Optics* 19 (04): 1.